

Large/small eddy simulations: A high-fidelity method for studying high-Reynolds number turbulent flows

Arnab Moitro,¹ Sai Sandeep Dammati,¹ and Alexei Y. Poludnenko^{1, a)}

School of Mechanical, Aerospace and Manufacturing Engineering, University of Connecticut, Storrs, CT 06269, USA

(*Electronic mail: alexei.poludnenko@uconn.edu)

(*Electronic mail: arnab.moitro@uconn.edu)

(Dated: 17 September 2024)

Direct numerical simulations (DNS) are one of the main ab initio tools to study turbulent flows. However, due to their considerable computational cost, DNS are primarily restricted to canonical flows at moderate Reynolds numbers, in which turbulence is isolated from the realistic, large-scale flow dynamics. In contrast, lower fidelity techniques, such as large eddy simulations (LES), are employed for modelling real-life systems. Such approaches rely on closure models that make multiple assumptions, including turbulent equilibrium, small-scale universality, etc., which require prior knowledge of the flow and can be violated. We propose a method, which couples a lower-fidelity, unresolved, time-dependent calculation of an entire system (LES) with an embedded Small-Eddy Simulation (SES) that provides a high-fidelity, fully resolved solution in a sub-region of interest of the LES. Such coupling is achieved by continuous replacement of the large SES scales with a low-pass filtered LES velocity field. The method is formulated in physical space, makes no assumptions of equilibrium, small-scale structure, and boundary conditions. A priori tests of both steady and unsteady homogeneous, isotropic turbulence are used to demonstrate the method accuracy in recovering turbulence properties, including spectra, probability density functions of the intermittent quantities, and sub-grid dissipation. Finally, SES is compared with two alternative approaches: one embedding a high-resolution region through static mesh refinement and a generalization of the traditional volumetric spectral forcing. Unlike these methods, SES is shown to achieve DNS-level accuracy at a fraction of the cost of the full DNS, thus opening the possibility to study high-Re flows.

I. INTRODUCTION

Turbulence is one of the most ubiquitous physical processes in the Universe: it controls the flow of nutrients in the living organisms¹, enables efficient combustion in engines², drives mixing and circulation in the planetary oceanic and atmospheric processes³, and plays one of the central roles virtually in all astrophysical contexts, from the birth of stars in turbulent interstellar clouds⁴ to their deaths in violent supernovae explosions⁵. Highly nonlinear dynamics of turbulence is often further complicated by the presence of other, tightly coupled physical processes. As a result, detailed understanding of such systems requires first-principles modeling by solving the governing equations for the full range of scales, which are dynamically important in a given system. In most cases, such range of scales is large, with the overall cost of a fully-resolved computation increasing with the Reynolds number⁶ as $O(Re^3)$, thus placing first-principles modeling of realistic systems outside the reach of modern computing.

Traditionally, there have been two paths to resolve this difficulty. The first path is to forego the resolution of small scales, focusing the computational resources on the system-specific large-scale dynamics, while capturing the effects of small scales with the appropriate subgrid-scale (SGS) models. This gave rise to a multitude of reduced-order methods, including Reynolds Averaged Navier Stokes (RANS), Large Eddy

Simulations (LES), etc.^{7–12} The second path concentrates the limited computational resources on fully resolving the small-scale flow structure in the context of Direct Numerical Simulations (DNS)¹³. Traditionally, DNS and the low-order methods have remained largely disconnected, even though their conceptual synergy is critical as the first-principles understanding provided by the DNS enables the development of the accurate SGS models, which are central to the reduced-order methods.

In order for the DNS to be able to both capture the dissipation range and also develop an inertial range within a computationally limited range of scales, the energy-generating large scales must be excluded from a simulation. This, however, immediately leads to two key limitations. First, when the DNS are disconnected from a realistic large-scale flow, they are typically restricted to more idealized, canonical configurations. Second, aside from a more specialized case of decaying turbulence, such idealized DNS must include a mechanism for generating and sustaining turbulence, thus mimicking the effect of the missing large scales that feed the energy to smaller scales. At the same time, a particular forcing method may not necessarily be physically equivalent to the action of large scales, and furthermore it can critically affect the structure of the resulting turbulence^{14–18}. As a result, any such external forcing must be treated carefully.

Over the years, a wide range of approaches for turbulence forcing have been introduced. Broadly, these can be divided into two classes: (i) generalized methods for canonical flows; and (ii) system-specific methods, which aim to incorporate the large-scale flow information. The first class treats forcing as

^{a)} Also at Department of Aerospace Engineering, Texas A&M University, College Station, TX, USA

a computational technique, which is intended to inject kinetic energy into the domain at a prescribed rate to sustain turbulence. Such methods are the simplest and most widely used, however the resulting forcing is idealized in nature, whose sole objective is to compensate the energy loss due to turbulent dissipation. As a result, they implement forcing without a connection to any particular large-scale flow. Thus, they crucially rely on the assumption of the universality of small scales, which are independent of the details of a large-scale flow.

Such generalized forcing techniques involve two major subclasses: volumetric and boundary forcing. One of the earliest methods for direct volumetric forcing is based on turbulence stirring in spectral space. A method proposed by Eswaran and Pope¹⁹ (also see Lemaster and Stone²⁰) is based on the stochastic forcing of the smallest wavenumbers of the flow. Similar approach has also been used, for example, by Seror *et al.*²¹, which is based on replenishing the dissipated energy back at the large scales, by Siggia and Patterson²², which freezes the Fourier coefficients of velocity at low wavenumbers, and by Carati, Ghosal, and Moin²³, which apply forcing proportional to the velocity in the wavenumber space. Broadband spectral-space forcing methods have also been proposed²⁴, which multiply the Fourier coefficients of the velocity in a chosen wavenumber range by a scalar to compensate for the energy dissipation.

The main advantage of such spectral forcing techniques is their ability to target specific scales for energy injection with a precisely defined energy injection spectrum. While such approaches are natural for solvers operating in the Fourier space, for physical-space solvers they introduce significant cost of the Fourier transforms, and their implementation can be non-trivial in the domains with non-periodic boundaries or complex geometry. These limitations are partially addressed by the methods, which apply volumetric forcing directly in physical space. For instance, linear forcing, proposed by Lundgren²⁵ for incompressible flows, and later extended by Rosales and Meneveau²⁶, applies a forcing term proportional to the velocity at every point in the domain. This approach is simple to implement but it energizes all wavenumbers, which at least in principle implies that the inertial range dynamics is no longer independent of driving. An extension of linear forcing has also been proposed²⁵, which applies forcing only to the small wavenumbers, however, it requires low-pass filtering of the velocity field. Linear forcing method was further extended to compressible flows by Petersen and Livescu²⁷, who introduced separate coefficients to force the solenoidal and dilatational components of the velocity field. This, however, also requires the Fourier decomposition of the velocity field, and thus it sacrifices the simplicity of linear forcing, restricting the method to periodic domains. Moreover, for all types of linear forcing, the resultant driving is isotropic, and extensions to inhomogeneous flows and non-periodic domains are not straightforward.

The second sub-class of the generalized forcing methods involves approaches, which rely on the boundary, rather than volumetric, forcing. These techniques generate shear-driven turbulence by superposing small fluctuations over an initial

flow and allowing turbulence to evolve^{28,29} in the presence of a globally imposed velocity gradient. Similar methods, known as the shearing box approximation, are also used to model turbulence in various differentially rotating astrophysical systems, e.g., accretion disks³⁰ and stellar interiors³¹. All such methods, however, provide less control over the resulting turbulence properties compared to the volumetric forcing, and they also introduce by design significant mean shear, which may not be always desirable. Furthermore, such shear-driven turbulence may require significant amount of time to develop, which can restrict the accessible range of Reynolds numbers and exacerbate the computational cost.

The generalized forcing techniques described above form the cornerstone of the existing studies of the canonical flows, in particular homogeneous, isotropic (HIT) and shear-driven/wall-bounded turbulence. At the same time, they suffer from two key limitations. First, they are restricted to just a few idealized flow configurations, which may not represent the full richness of possible turbulent flow conditions present in realistic systems. Second, such DNS can achieve only moderate Reynolds numbers with the computational cost growing rapidly as $O(Re^3)$. For instance, largest DNS to-date of the HIT reach the Taylor-scale Reynolds number³² of $Re_\lambda = 1300$, which requires an extremely large grid $N^3 = 12,288^3$. Similarly, the largest DNS of a turbulent channel flow has a friction Reynolds number, $Re_\tau = 5200$ and the grid size of $10,240 \times 7,680 \times 1,536$ ³³. Such turbulent conditions, which are at the limit of what is possible with modern computing resources, are still far from the realistic turbulent flows even in engineering systems, let alone atmospheric or astrophysical environments. As a result, modern DNS are not able to address many open questions regarding the nature of high- Re turbulence.

Contrary to the methods described above, which are decoupled from any external flow, the second major class of turbulence forcing techniques aims to either (i) drive the fully resolved flow solution using a realistic model of the large scales of a particular flow of interest or (ii) by directly embedding the high-fidelity solution in a large-scale flow. An example of the former is a method proposed by Rah, Dhanda-pani, and Blanquart³⁴, which focuses on the flow in turbulent round jets, with the forcing term based on the mean centerline jet velocity. Although this method achieves forcing, which is anisotropic and is based on an experimentally determined external flow field, it is only applicable in triply periodic domains for a particular region of the jet, and the forcing parameters must be determined individually for other regions of interest or for different flow configurations. An example of a direct embedding approach was described by Elnahas, Lozano-Duran, and Moin³⁵, who applied a DNS patch in the near-wall region of an LES of an incompressible channel flow to serve as the wall model. Statistical quantities from the LES were used to provide the large-scale flow information for the DNS, while the DNS data were used to obtain the wall shear stress for the LES. Overall, both of these methods are developed with the aim of capturing a specific flow, whether it is a jet or a wall-bounded flow.

Hybrid LES-DNS methods, analogous to the approach of

Elnahas, Lozano-Duran, and Moin³⁵, have also been proposed for planar jets and decaying turbulence, where a certain sub-region in an LES is refined to the DNS resolution using static (SMR) or adaptive mesh refinement (AMR) techniques^{36,37}. The embedded high resolution sub-region is not forced in any special way with the kinetic energy from large scales in the LES entering it via the boundaries, thus effectively forcing this region. These studies, however, primarily aim at training machine learning algorithms to obtain LES closures, and thus they focus on the large-scale or mean-flow behavior, such as the resolved kinetic energy spectra, mean dissipation, or mean streamwise jet velocity, rather than on the accuracy of the small scales in the refined region. Other studies^{38,39} have also described such direct AMR-based embedding of a high-fidelity solution, in particular focusing on exploring optimal characteristics of the mesh refinement approaches, such as the interpolation and integration schemes or the coarse-fine transition-zone depth.

This second class of turbulence forcing methods partially addresses one of the major limitations of the generalized forcing techniques described above by directly injecting the large-scale flow information in the small-scale calculation, and thus at least potentially allowing one to treat arbitrary large-scale flows. At the same time, the ability of such methods to provide DNS-level solution accuracy in the general case, especially in terms of the higher-order metrics, and most importantly, their ability to reach high Reynolds numbers beyond what can be achieved in the traditional DNS, has not been established.

It is also worth noting that atmospheric modeling community has employed a range of multi-fidelity approaches, which also aim to couple a low-fidelity, large-scale flow information with a higher fidelity small-scale calculation, albeit not a DNS. For instance, spectral nudging techniques^{40–42} use the large-scale data obtained from a global reanalysis model for forcing specific wavenumbers in the interior of a smaller regional model. Regional modelling is treated as a downscaling problem, as it incorporates large-scale information while allowing small-scale dynamics to develop. Similar method has also been applied outside of weather modelling, for example to infer physical parameters in turbulent flows⁴³. While providing a great deal of flexibility in incorporating the large-scale flow information, spectral nudging also has several important limitations. First, it operates in spectral space, and extensions to physical space on the non-periodic domains are not straightforward due to the requirement of spectral decomposition of various modes. Furthermore, this approach generally does not aim to achieve DNS-level fidelity of the small-scale solution, and its ability to provide such level of accuracy has largely not been explored. Finally, in recent years, attempts have been made to extend nudging techniques, as a form of data assimilation, from the traditional weather modeling to more fundamental turbulence studies^{44,45}.

Other methods employed in weather modelling, similar to spectral nudging, include super-parameterization techniques^{46,47}, in which a simulation with a finer resolution is embedded in a large-scale calculation and forced volumetrically using mean velocities and gradients obtained from the latter. As in spectral nudging, the goal is not to achieve DNS-

level small-scale solution fidelity, but rather enable coupling between various subgrid parameterizations and observe their effects on the large scales. Furthermore, such methods have been demonstrated only for specific boundary conditions and they only ensure that the small-scale fields match the large-scale solution on average. As in the case of other embedding methods described above, super-parameterization approaches cannot ensure a high-level of accuracy for the small scales or provide exact closures for an LES.

Finally, we note that a method for performing a resolved simulation, albeit for a short duration to obtain turbulence statistics, using initial conditions from the LES data has been proposed by Yeung and Ravikumar⁴⁸. It requires, however, a fully resolved simulation to be set up in the entire LES domain, which can be computationally prohibitive for the problems of engineering relevance, even if performed for a short duration.

Here we aim to combine the strengths, while addressing the limitations, of these two classes of turbulence forcing methods by formulating a general approach to perform fully resolved simulations of turbulence in a sub-region of interest of an arbitrary large-scale flow, as illustrated in Fig. 1. In particular, the key three requirements of the proposed method are:

1. It should be able to recover the actual instantaneous, as well as the time-averaged or statistically representative, small-scale structure in a particular region of the larger-scale flow. Such embedded calculation must provide the solution accuracy comparable to that of the DNS in terms of all turbulence metrics, from the global ones to the higher-order ones reflective of the nonlinear turbulent structure. Ability to recover instantaneous fields, although a stringent requirement, can be desirable in many practical situations, e.g., reacting flows, where instantaneous deviations of the velocity gradients from their mean may result in local rapid mixing of the reactants, auto-ignition, etc.
2. No prior knowledge of the overall flow structure should be required, including assumptions of homogeneity, isotropy, equilibrium, or small-scale universality.
3. In order to be useful in the studies of practical flows, proposed method should be formulated in physical space, and it should be applicable for arbitrary initial and boundary conditions, as well as system geometry.

Ultimately, the goal is to develop a method, which will be able to achieve practically relevant turbulent Reynolds numbers in a fully resolved simulation beyond what is accessible in modern DNS.

Considering these objectives, we introduce a multi-fidelity simulation method, which starts with a lower-fidelity, time-dependent calculation of the flow of interest, in which a smaller region is identified based on its dynamical, physical, or other properties for high-fidelity modeling. The key requirement for this under-resolved calculation is that it captures the large-scale flow structure with the desired accuracy. Fidelity of the small scales in this calculation is not essential, so

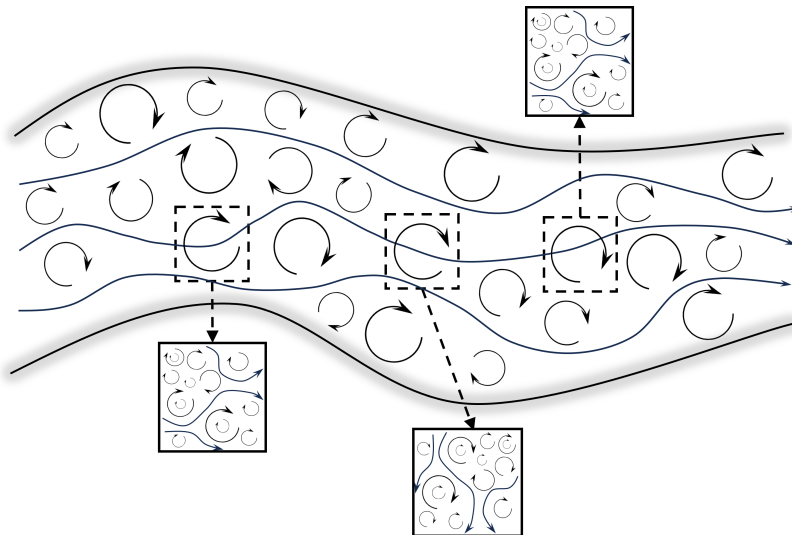


FIG. 1. L/SES concept. Large scales of a complex flow are captured by the low-cost, low-fidelity simulation. Detailed small-scale structure in the chosen regions of interest is then obtained using the L/SES method.

long as the inaccuracies in the small-scale solution do not degrade the accuracy of the large-scale flow. While in this work we primarily focus on the LES for such large-scale calculations, other lower fidelity alternatives, e.g., unsteady RANS, can also be considered in the future as they can further reduce the cost of the proposed method, thus increasing its practical utility. Flow data is extracted by low-pass filtering the velocity field in the sub-region of interest in the LES, and it is used to force the companion high-fidelity Small Eddy Simulation (SES), which resolves all small scales and uses the LES data as an effective model for the large scales.

Resulting Large/Small Eddy Simulation approach, or L/SES, can be viewed as a generalization of the second class of forcing methods, which aim to inject the actual large-scale flow structure into the high-fidelity simulation. At the same time, as will be shown in the discussion below, proposed method differs in several key aspects from the approaches discussed above. In particular, L/SES employs both boundary and volumetric forcing, which we find to be critical to achieve high solution accuracy. Furthermore, in contrast to the spectral nudging approaches, L/SES is formulated in physical space for complex domains with non-periodic boundaries, where Fourier decomposition would not be practical. As a result, L/SES relies on explicit filtering to separate different spectral components and thus to provide volumetric forcing formulated in physical space. Finally, in contrast to the traditional data assimilation approaches, in particular nudging techniques, which aim to inject the true reference flow field (obtained in experiments, observations, or another high-fidelity simulation) in order to achieve synchronization between such true data and the obtained solution, L/SES sets effectively an opposite goal. It crucially relies on a low-fidelity reference solution. Thus, we aim to demonstrate that using such low-fidelity large-scale forcing data, it is possible to recover the small-scale flow field with high accuracy.

Below we describe the L/SES approach, and we validate

it for steady and unsteady HIT in an *a priori* sense, where the large-scale data is provided by filtered fields of a fully resolved large-scale DNS, rather than LES. Detailed *a posteriori* tests for a wide range of Re will be presented in the follow-up paper. We consider a range of metrics, including global kinetic energy content, time-averaged and time-dependent kinetic energy spectra, probability density functions (PDF) of the small-scale quantities, such as enstrophy and dissipation, as well as subgrid-scale dissipation, which is directly relevant for the LES closures.

We also contrast the L/SES with the two major types of turbulent forcing methods discussed above. First, we describe a generalization of the first class of turbulence forcing approaches, namely traditional volumetric forcing, in which the time-dependent energy injection rate is directly determined from the sub-region of interest in an LES instead of being prescribed as a free parameter. The small-scale calculation, which is intended to represent that LES sub-region, is then forced using the standard stochastic spectral forcing^{19,20,49}. While this method can capture some aspects of the time-varying evolution of the LES, the large-scale flow complexity is reduced to a single scalar parameter, similar to the traditional spectral forcing approach. Second, we also compare the L/SES flow solution with the SMR/AMR-based approach similar to those describe above^{36–39}, in which a high-resolution region is directly embedded in a low-fidelity simulation using static mesh refinement.

The remainder of the paper is organized as follows. Details of the L/SES method are described in § II. Alternative approaches, including the generalization of the stochastic spectral forcing and the SMR-based method, are summarized in § III. The numerical method as well as the details of the DNS, which provides the forcing data, and the associated SES are given in § IV. Comparison of various turbulence metrics for all three methods is presented in § V. We end with a discussion of the L/SES method, its implications for turbulence studies,

limitations, and open questions, in § VI, along with the concluding remarks.

II. LARGE/SMALL EDDY SIMULATION APPROACH

A. Method description

The key objective of the proposed L/SES approach is to utilize in the companion high-fidelity SES calculation the full large-scale flow-field information available in the LES. In other words, large scales in the SES should match the large-scale LES flow both at the boundaries and in the entire volume of the SES domain to ensure seamless transfer of the flow structure from the LES to the SES.

To achieve this, the SES solution is continuously adjusted to replace the flow structure produced by the SES on scales larger than a chosen filter scale, Δ , with the known ‘true’ large-scale LES flow field. A low-pass filtering operation is used to separate the large-scale from the small-scale components both in the LES and the SES. Mathematically, the i^{th} component of the velocity perturbations introduced in the SES is

$$\delta u_i = \tilde{u}_{i,LES} - \tilde{u}_{i,SES}, \quad (1)$$

where $\tilde{u}_{i,LES}$ and $\tilde{u}_{i,SES}$ are the LES and SES velocity fields, respectively, filtered at the scale Δ . Such velocity perturbations are then applied after each time step, giving the new SES velocity field at the time step $n+1$

$$u_{i,SES}^{n+1} = u_{i,SES}^n + \delta u_i = (u_{i,SES}^n - \tilde{u}_{i,SES}^n) + \tilde{u}_{i,LES}^n. \quad (2)$$

This operation removes the large-scale component of the SES flow field ($\tilde{u}_{i,SES}^n$ term) and replaces it with the large-scale velocities from the LES. Thus, the resulting field is a superposition of small scales produced by the SES (term in the parenthesis) and the large scales of the LES. We emphasize that low-pass filtering ensures that all LES scales $> \Delta$, including ones larger than the SES domain size L_{SES} , are involved in driving the SES solution. Formally, this formulation is equivalent to the traditional nudging techniques⁴⁴ with an important distinction, which concerns the reference solution. While in the data assimilation approaches it represents true data, typically obtained in experiments or observations, in L/SES it is a low-fidelity solution, in which only the large-scale component can be assumed to be accurate.

Here we are considering weakly compressible flows with the turbulent Mach number $Ma_t \sim 0.05$. Therefore, forcing the velocity field is sufficient. At the same time, for compressible flows, momentum should be perturbed instead through a similar procedure

$$\delta(\rho u_i) = \overline{(\rho u_i)}_{LES} - \overline{(\rho u_i)}_{SES}, \quad (3)$$

where $\overline{(\rho u_i)} = \bar{\rho} \tilde{u}_i$, and $\overline{(\dots)}$ denotes Reynolds filtering.

In the proposed approach, there are three key parameters, which need to be chosen appropriately:

- *Filter scale, Δ* : In the explicitly filtered LES, Δ is set by definition. In the implicitly filtered ones, Δ needs to be chosen sufficiently larger than the LES grid size, dx_{LES} , to ensure that all scales $> \Delta$, which will be passed to the SES, are minimally affected by any grid effects and the associated numerical dissipation. As a result, specific choice of Δ would depend on the details of the numerical solver employed. For the finite-volume, Godunov-type solver used here, which is based on the constrained transport upwind (CTU) scheme with the piecewise-parabolic (PPM) spatial reconstruction^{50–52} (also see § IV A below), we find $\Delta \sim 16dx_{LES}$ is an appropriate choice.
- *SES domain size, L_{SES}* : Criteria for choosing L_{SES} are two-fold. On one hand, L_{SES} must be close to Δ to minimize the computation cost since scales $> \Delta$ are replicated from the LES. On the other, some overlap between Δ and the largest SES scales is necessary to ensure that the SES field is consistent with the LES and the overall method is stable. We find that the choice of $L_{SES} = 2\Delta$ provides optimal results while minimizing the range of scales covered both in LES and SES.
- *SES grid resolution, dx_{SES}* . Since the goal of the SES is to resolve fully all dynamically important flow scales, the choice of dx_{SES} would typically be governed by the physics of the flow of interest. In the case of non-reactive, homogeneous, isotropic turbulence, which we consider in the tests described below, natural choice is $dx_{SES} = \eta/2$, where η is the Kolmogorov scale of the flow. Such resolution was shown in prior studies to be sufficient to capture turbulence structure accurately near the dissipative scale^{53–55}. The caveat is that in the unsteady, non-equilibrium turbulent flows, such as considered in one of the tests described below, η can vary in space and time, and thus the choice of dx_{SES} must either be made conservatively or the time-varying SES resolution must be implemented.

The best performance of the method is expected when both Δ and L_{SES} are $\gg dx_{SES}$, i.e., in the flows with sufficiently large Re_λ . In particular, in the SES, sufficient separation must exist between the dissipative and forcing scales to allow small scales to develop proper physical dynamics, which is not simply an imprint of the large-scale forcing by the LES flow field. Furthermore, when dx_{SES} is close to dx_{LES} , LES can be viewed just as an under-resolved DNS, and the combined cost of L/SES will be comparable to that of a DNS.

Finally, we note that the approach described here implements one-way coupling between the large and small scales. This places constraints on the types of flows, which can be studied using the L/SES. In particular, large scales must not be controlled by the small-scale dynamics, more specifically, there should not be a pronounced up-scale energy transfer from the small scales^{56–58}. Extension of the L/SES method to a two-way coupled approach, in which SES effectively constrains the LES closures, is the subject of future work.

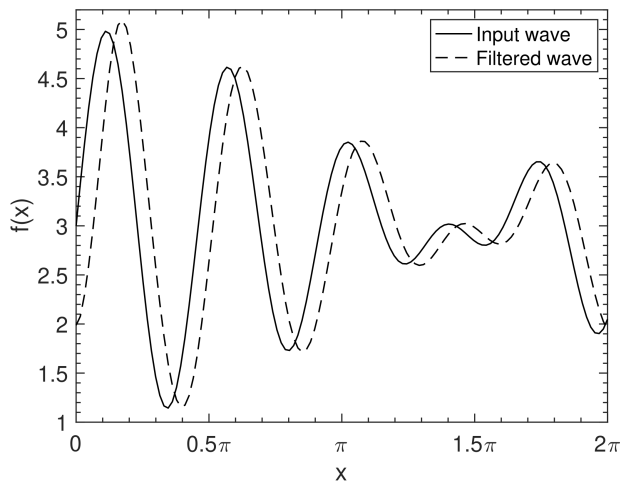


FIG. 2. Phase shift caused by the 4th-order Chebyshev filter.

1. Filter choice

One of the key steps in the L/SES approach is the low-pass filtering, which isolates the large-scale flow structure in the LES and SES. An appropriate choice of such filter is critical both for the accuracy and stability of the overall method. In particular, the filter must exhibit the following four characteristics:

1. *Spectral sharpness*: The filter must provide a spectral response as sharp as possible.
2. *Spatial locality*: The filter should also be local in space or, more specifically, it should have compact support. A non-local filter, such as the Fourier-transform-based spectral filter, when applied on a non-periodic domain would produce aliasing errors, which would affect the small scales disproportionately as they have inherently lower energy. Furthermore, a local filter is computationally more efficient.
3. *Zero phase shift*: The filter should not produce a phase shift in the filtered variables. The LES and SES velocity fields are comprised of a wide range of wavenumbers. Filters with a non-zero phase response would cause motions at different scales, i.e., with different frequencies, to separate and create sharp gradients, thus destabilizing the overall method. An example of such dispersion is shown in Fig. 2 for the 4th-order Chebyshev type-II filter⁵⁹. In particular, shown is a low-frequency one-dimensional (1D) sinusoidal input wave (solid line), which lies in the pass band of the filter, similar to an LES flow field, along with its filtered output (dashed line). Since the input signal does not have any high-frequency component, the filtered output should coincide with the input. Instead, the phase-shift caused by the filter results in a non-zero velocity perturbation δu , calculated by the subtraction of these two waves. Such non-zero δu , if injected into an SES calculation, would destabilize it breaking the solution.

4. *Commutativity*: Finally, an additional property to consider while choosing an appropriate filter is its commutativity with the derivative operators. Although this is not strictly necessary for the L/SES, this property is desirable if the same filter were to be used also as an explicit LES filter.

Fourier-transform-based spectral filter would naturally provide the sharpest spectral response. At the same time, we seek a general method, which should be practical in non-periodic domains, ideally with an arbitrary geometry. While spectral filter can be applied directly in physical space, it is non-local and in a non-periodic domain it would produce a phase shift, which destabilizes the solution. Therefore, here we adopt a higher-order differential filter of the form

$$\phi = \bar{\phi} + (-1)^{n/2} a^n \nabla^n \bar{\phi}, \quad (4)$$

where n is the filter order, ϕ is a variable being filtered, $\bar{\phi}$ represents the filtered value, ∇ is the usual differential operator, and $a = \Delta/\sqrt{40}$ is the filter parameter chosen such that the filter transfer function becomes 0.5 at the cutoff width Δ .⁶⁰ The 2nd-order version of this filter, i.e., for $n = 2$, was proposed by Germano⁶¹ for LES. This filter, although implicitly defined and computationally expensive, is chosen because it is local in space, and it gives both monotonic and non-dispersive frequency response. Furthermore, we use density-weighted Favre filtering $\tilde{u}_i = \bar{\rho} u_i / \bar{\rho}$. This, along with eq. (3), allows this method to be applicable also in the compressible flow regimes.

The transfer function of the above filter is

$$\hat{f}(k) = \frac{1}{1 + a^n k^n}, \quad (5)$$

which can be found using the Laplace transform of eq. (4). Here k is the wavenumber, and a is defined in eq. (4) above.

Figure 3(a) shows the compensated kinetic energy spectrum (solid line) in the DNS of HIT turbulence, described below, with the spectra of the same velocity field filtered using the 2nd-, 4th-, and 8th-order differential filter given by eq. (4). Dashed red line shows the result for an ideal spectrally sharp filter. Figure 3(b) shows the corresponding transfer functions for these three differential filters. For all filter orders, not all small scales below the filter width Δ are removed, while some scales $> \Delta$ are suppressed. Crucially, such spectral leakage decreases considerably from the 2nd- to 8th-order filter as the transfer function becomes progressively narrower in the wavenumber space.

Such non-ideal spectral response of the filter introduces errors in the velocity or momentum perturbations injected into the SES calculation (eqs. 1 or 3). In particular, eq. (1) can be re-written for the actual injected velocity perturbations as

$$\delta u_i = \left\{ (\tilde{u}_i^*)_{LES} - (\tilde{u}_i^{LS})_{LES} + (\tilde{u}_i^{SS})_{LES} \right\} - \left\{ (\tilde{u}_i^*)_{SES} - (\tilde{u}_i^{LS})_{SES} + (\tilde{u}_i^{SS})_{SES} \right\} \quad (6)$$

$$\approx (\tilde{u}_i^*)_{LES} - (\tilde{u}_i^*)_{SES} - (\tilde{u}_i^{SS})_{SES}. \quad (7)$$

Here, \tilde{u}_i^* represents the velocities filtered with an ideal spectrally sharp filter, while \tilde{u}_i^{LS} and \tilde{u}_i^{SS} represent the suppression of large scales $> \Delta$ and enhancement of small scales

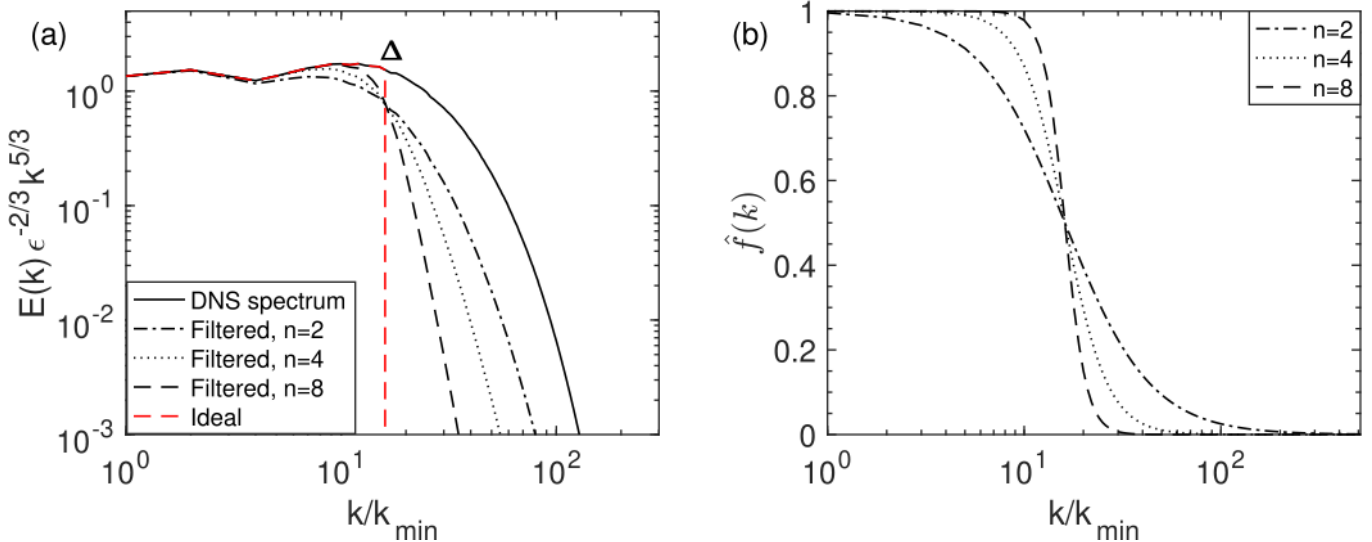


FIG. 3. (a) Spectral leakage in the differential filter at various filter orders. (b) Transfer functions of the differential filters of orders $n = 2, 4,$ and 8 given by eq. (4).

$< \Delta$, respectively, due to the spectral leakage in LES and SES (Fig. 3). Since in the LES small scales $< \Delta$ are either completely absent, or they are suppressed due to the lack of resolution, the term $(\widetilde{u}_i^{SS})_{LES}$ can be viewed as small. On the other hand, since large scales $\gtrsim \Delta$ are close in LES and SES by design, terms $(\widetilde{u}_i^{LS})_{LES}$ and $(\widetilde{u}_i^{LS})_{SES}$ approximately cancel each other. Therefore, spectral leakage will result in a systematic error $(\widetilde{u}_i^{SS})_{SES}$ in the velocity perturbations, which will effectively act to modify the small scales in the SES degrading (or in some cases, destabilizing) the solution. Hence, there is a need to select the filter carefully.

In the numerical tests discussed below, we use the 8th-order differential filter. While higher-order filters can be constructed, they would require a significantly larger stencil while only marginally improving the spectral response. Thus, the choice of $n = 8$ was found to be optimal. Resulting filter satisfies other requirements outlined above. In particular, it is spatially local as it can be calculated for each cell using a finite width stencil. And it has zero phase response, as the imaginary part of the transfer function in eq. (5) is zero.

Since solving the implicit eq. (4) in three dimensions (3D) is computationally expensive, we implement the filter in a directionally split way with the data being filtered in 1D successively along all three directions, as suggested by Edoh *et al.*⁶². In 1D, the resulting diagonally dominant sparse system of linear equations is solved directly using LU decomposition. A 2nd-order, central, finite difference operator is used to discretize eq. (4).

2. SES boundary conditions

The L/SES approach can be viewed as the volumetric forcing since velocity (or momentum) perturbations are applied throughout the entire SES domain. At the same time, since

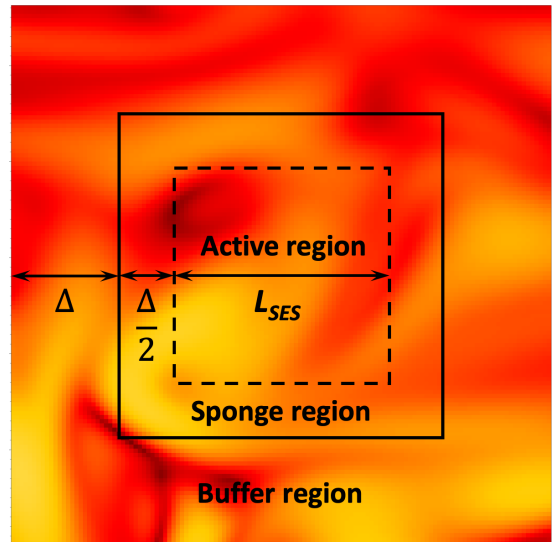


FIG. 4. SES domain showing the sponge, buffer, and active regions.

the SES represents a sub-region of the LES, its domain is not periodic. This raises the question of the appropriate boundary conditions treatment in the SES.

SES boundary conditions for all conserved variables are set directly using filtered LES data to ensure that at all times SES solution is fully consistent with the filtered LES field at the boundaries. To achieve this, SES solution is gradually relaxed to the filtered LES field using a sponge region near all boundaries. Such filtered LES field is constructed from the filtered LES density, pressure, and momenta, $\bar{\rho}$, \bar{P} , and $\bar{\rho}u_i$. Thus, the SES domain, which is evolved in the calculation, includes the sponge region and is thus larger than the active region of interest (see Fig. 4). As a result, since the filtered LES solution is injected throughout the SES volume, and it is also imposed

at the SES domain boundaries, the L/SES approach can be viewed as a combination of forcing both at the physical and spectral boundaries.

The sponge relaxation function used in the tests described here has the exponential form

$$f = \exp\left(\frac{1-j}{M}\right)(\bar{\phi}_{LES} - \phi_{SES}), \quad (8)$$

where j is the index of a cell from the nearest sponge region boundary (solid black line in Fig. 4), ϕ_{SES} is any conserved variable in the SES (note that the total energy is not filtered directly, but obtained from the filtered pressure and momenta), $\bar{\phi}_{LES}$ is the filtered LES value of the same conserved variable at that location, and M is the sponge layer parameter, which is taken to be equal to 3 following Marbaix *et al.*⁶³. This value of M was found to give the optimal results. Resulting quantity f is then added to all conserved variables in the sponge region modifying each variable as $\phi' = \phi + f$. Other forms of the sponge relaxation function can be employed, for instance, based on the quadratic polynomials⁶³

$$f = (x/D_s)^2(\bar{\phi}_{LES} - \phi_{SES}), \quad (9)$$

where x is the distance of a cell in the sponge to the nearest active region (dashed black line in Fig. 4) and D_s is the width of the sponge region.

The sponge region alone, however, does not address another important aspect related to the boundary conditions. Note that the filter is given by the inhomogeneous Helmholtz equation (4), the unique solution of which formally requires a boundary condition at infinity. Prescribing such a boundary condition is not possible on a finite discrete mesh. Therefore, the boundary will always introduce an error, unless the boundary is periodic, which is not the case in general since the SES flow field is non-periodic.

In principle, the non-periodic boundary can be treated by reducing the filter width near the sponge region boundaries. Such approach, however, is not ideal as in this case the filtered SES field will include smaller scales near the outer boundary of the sponge region. This will lead to systematic errors in the forcing term and a mismatch between the SES and the LES solutions at the boundary. Resulting errors can advect into the active region and destabilize the overall SES solution.

To address this difficulty, an additional buffer region is created outside of the sponge region (cf. Fig. 4). Such buffer is filled at every time step directly with the LES filtered data, as described above. Periodic boundary condition is assumed at the outer boundary of the buffer. This eliminates the need to reduce the filter width, and the entire domain, which includes active, sponge, and buffer regions, can be filtered with a constant filter width. Furthermore, buffer region also pushes the domain boundary further away from the active region, minimizing the errors introduced into it. In particular, since even the extended SES domain with the buffer is non-periodic, using periodic boundary condition, as well as any other boundary condition not at infinity, will create errors in the filtered result. However, if the buffer region is sufficiently large, these errors primarily affect the buffer, where

they are discarded. Furthermore, although the appended data is taken from a large-scale simulation, which does not contain a small-scale component, this does not affect the filtering, as the filter is low-pass in nature and it is aimed at removing the higher wavenumbers. Finally, Navier-Stokes equations are not solved in the buffer, and thus the additional computational cost of including the buffer is modest amounting only to the extra cost of filtering in that region as well as the additional memory cost.

Figure 5a shows comparison of the effect of the two sponge functions (eqs. 8 and 9) on the accuracy of the filtering of a synthetic 1D signal. The input signal (solid red and blue lines in panel a) is comprised of the low-frequency component, analogous to the LES field, which is given by the function $f_{low}(x) = 6 + 2 \sin(0.9x)$ and which extends through the entire domain. This input signal also has a high-frequency component, analogous to the SES field, given by the function $f_{high}(x) = \sin(8.8x)$. This high-frequency component is present in the central active region, and it is damped in the sponge region (shaded light gray areas) using either exponential (solid red line, eq. 8) or quadratic (solid blue line, eq. 9) functions. Only the low-frequency component is present in the buffer region (shaded dark gray areas). Note that both signal components are non-periodic in the domain being considered. The result of filtering the input signal damped using the two sponge functions is shown with the dashed red and blue lines, which are indistinguishable from the low-frequency reference signal in the active and sponge regions. Filtering successfully preserves the low-frequency component and removes the high-frequency component in the central region, with deviations from $f_{low}(x)$ occurring only in the buffer, in which they become pronounced near the outer boundaries.

More quantitative comparison is given in Fig. 5b, which shows the relative error between the filtered output signal and the reference low-frequency input signal $f_{low}(x)$. Both sponge functions give very similar results, and thus we choose to employ the exponential sponge function for all the tests discussed below.

Figure 5 also demonstrates the effect of the sponge and buffer region sizes. In particular, in panels (a) and (b), the sponge and buffer region widths are $\Delta/2$ and Δ , respectively. The resulting relative error is $\sim 10^{-3}$ in the active region and it gradually increases through the sponge and buffer regions exceeding 10% near the boundaries. Increasing the sponge region size by a factor of four to 2Δ (Fig. 5c) somewhat reduces the relative error in the active region to below 10^{-3} , while the error in the buffer region remains approximately the same. In contrast, increasing the buffer region size by a factor of four to 4Δ (Fig. 5d) does not change the relative error in the active and sponge regions, though error in the buffer region decreases by about an order of magnitude. Decreasing the sponge and buffer region sizes below $\Delta/2$ and Δ , respectively, increases filtering errors substantially.

Therefore, sponge and buffer region sizes shown in Figs. 5a,b, namely $\Delta/2$ and Δ , respectively, represent the optimal balance between the resulting error and the associated computational and memory costs. Such sizes are used in all tests discussed below, and they are found to provide good

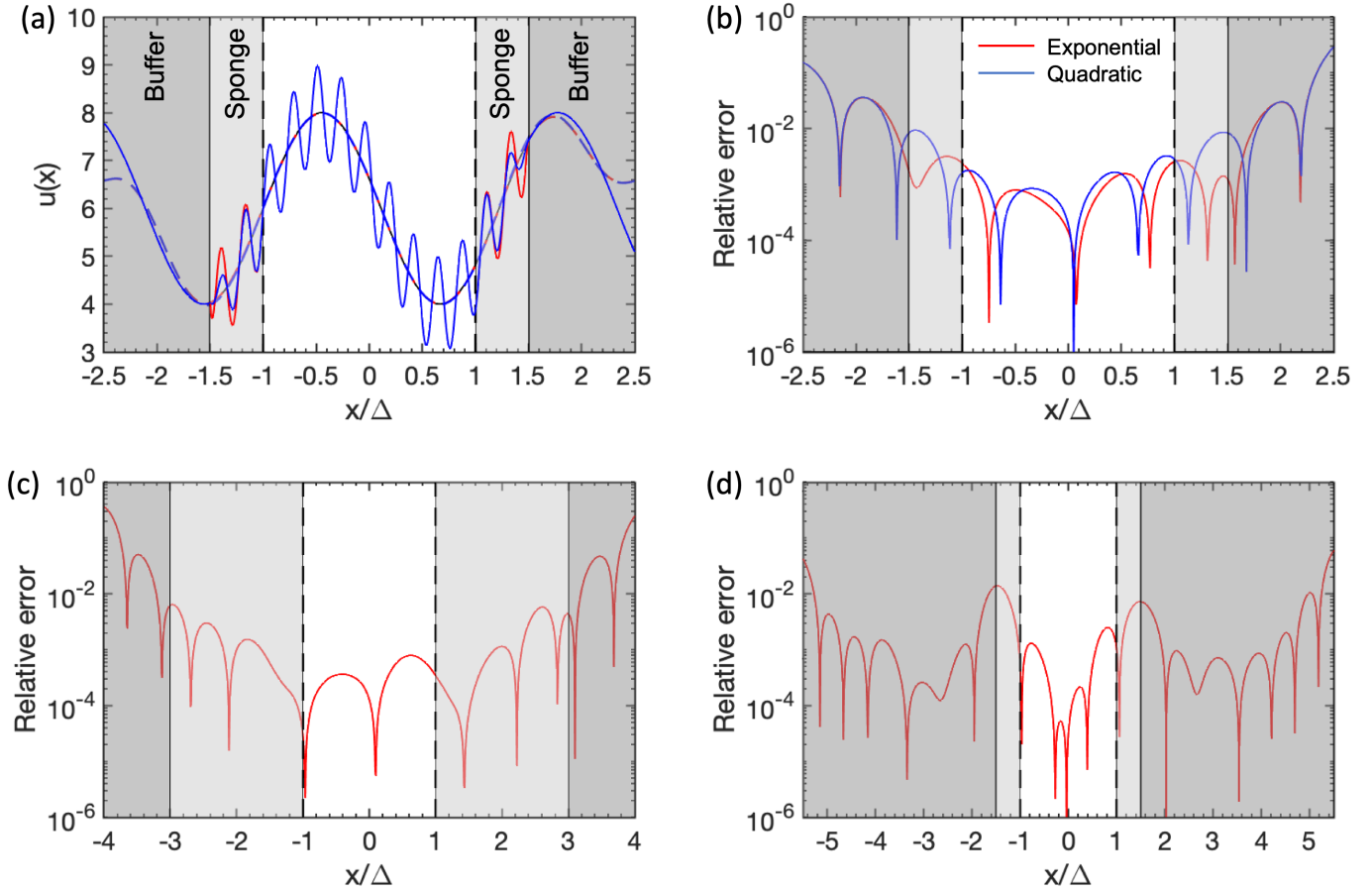


FIG. 5. Comparative tests of the sponge function type as well as the width of the sponge and buffer regions. a) Synthetic input signal with a high-frequency component in the active region damped in the sponge region using exponential (solid red line, eq. 8) and quadratic (solid blue line, eq. 9) sponge functions to the reference low-frequency signal. Filtered signal is shown with the dashed lines. b) Relative error between the filtered output signal and the reference low-frequency signal for the exponential (red line) and quadratic (blue line) sponge functions. Sponge region (shaded light gray) width is $\Delta/2$ and buffer region (shaded dark gray) width is Δ . c) Effect of the sponge region with $4\times$ larger width 2Δ on the relative error of filtering. d) Effect of the buffer region with $4\times$ larger width 4Δ on the relative error of filtering. See text for further details.

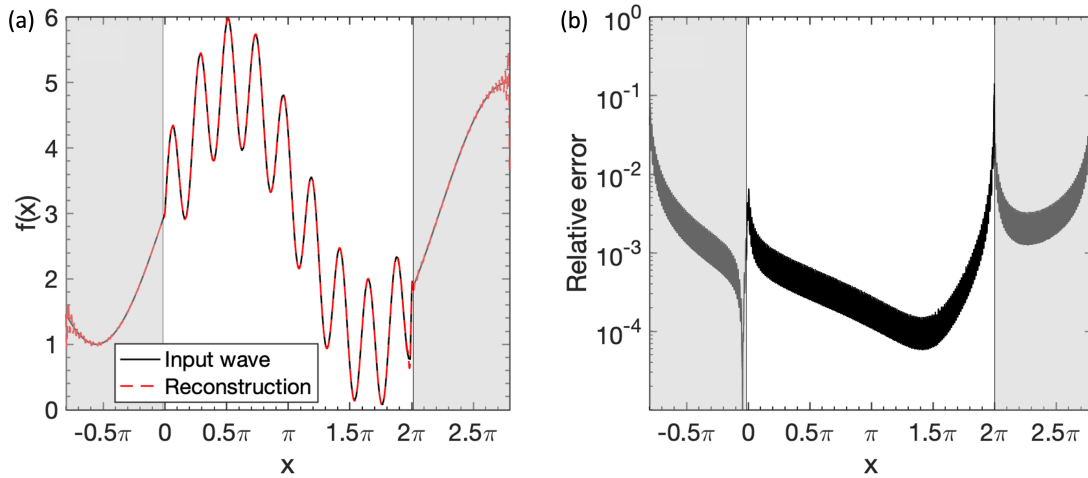


FIG. 6. (a) Spectral (trigonometric) spatial interpolation of a non-periodic, bi-modal 1D signal (cf. Fig. 5). (b) Relative error of the interpolation. The non-shaded area represents the entire SES domain (including sponge and buffer regions), while the shaded areas represent additional regions included only in the interpolation.

overall stability and accuracy of the SES.

3. Spatial and temporal interpolation

As discussed in § II A, velocity or momentum perturbations in eqs. (1) or (3) are applied in SES at every timestep and in every cell. Since SES by construction has finer spatial and temporal resolution than LES, the filtered LES forcing field must be interpolated both in space and time. Traditional interpolants, such as trilinear or cubic spline, introduce spurious oscillations in the spatially interpolated velocity field at higher wavenumbers. Such oscillations were found to be detrimental to the SES accuracy as they are retained in the forcing field throughout the simulation, and they affect the very scales that we seek to capture.

If the large-scale data, which is used to drive the SES calculations, are periodic, as in the DNS used in the *a priori* tests described below, spectral interpolation represents the most accurate approach. In particular, the Fourier transform of the filtered large-scale field is first obtained. Resulting field, which lacks scales smaller than the filter scale Δ , is then padded with zeros at the higher wavenumbers present in the SES, and the inverse Fourier transform is performed. Resulting spatially interpolated velocity field is ensured to contain no small-scale component.

The entire procedure is equivalent to the trigonometric interpolation⁶⁴. Although this procedure is applied here via Fourier transforms, it can be performed directly in physical space⁶⁵. While ideally it would require periodic data, it can also be applied to non-periodic LES domains. The original spectral content would be preserved by the operations and mild distortions of the data would occur near the domain edges. The distortions can be mitigated by adding a few extra points to the SES domain size (including the buffer), performing the interpolation on this extended grid, and later discarding the excess interpolated data outside the SES domain. Figure 6 illustrates the accuracy of this procedure applied to a non-periodic synthetic 1D data represented by the same bimodal sine wave as in Fig. 5. The ratio of the resolution (or step size) between the coarser input and the finer output signals is 8. Setting the number of extra points on each side of the domain boundary to be twice the ratio of the grid spacing between the coarse and fine data proves to be sufficient to eliminate the distortions. Figure 6b shows that the relative error of the interpolation is the largest in this added region (shaded gray area) and near the boundaries of the central region, which in the SES would lie in the buffer region, and hence would not affect the SES solution. Otherwise, the relative error is $\lesssim 10^{-3}$, which is comparable to the filtering errors shown in Fig. 5.

Finally, the filtered and spatially interpolated LES flow field also has to be interpolated in time to provide forcing data at each finer SES time step. For the present tests, linear interpolation proved to be sufficient. While ideally, such interpolation would be done between each successive LES time steps, it may be too costly computationally to filter and interpolate LES data so frequently especially in compressible solvers, in

which the time step is constrained by the sound speed rather than the flow velocity. We find that a much larger time interval for the forcing LES data is sufficient

$$\Delta t_{forcing} \lesssim \frac{\Delta}{U_{rms}}, \quad (10)$$

where Δ again is the filter scale, and U_{rms} is the r.m.s. velocity in the region of interest. This effectively represents a characteristic filter-scale crossing time by the flow, which means that the changes in the large-scale flow structure are minimal on this timescale. As a result, snapshots of the flow-field taken at this time interval will be close to each other, and thus one can interpolate between them in time with a minimal loss of accuracy.

In the case of an explicit compressible solver, such as used in this study, the time step of the LES calculation is constrained by the Courant-Friedrichs-Lewy condition

$$\Delta t_{LES} \approx \text{CFL} \frac{\Delta x_{LES}}{(U_{rms} + c_s)}, \quad (11)$$

where c_s is the sound speed and $\text{CFL} \sim O(1)$ is the Courant-Friedrichs-Lewy number. Then

$$\frac{\Delta t_{forcing}}{\Delta t_{LES}} \lesssim \frac{1}{\text{CFL}} \frac{\Delta}{\Delta x_{LES}} \left(1 + \frac{1}{M_{rms}}\right). \quad (12)$$

Here $M_{rms} = U_{rms}/c_s$. For the low-Mach-number turbulence with $M_{rms} < 0.1$, and assuming the ratio of the filter scale to the LES cell size $\Delta/\Delta x_{LES} \gtrsim 10$, this relation suggests that LES data for forcing the SES can be collected every $\gtrsim 100$ time steps or even less frequently. As a result, the cost of LES data filtering and interpolation becomes negligible compared to the overall computational cost of the LES calculation. This consideration applies both to the SES performed synchronously with the LES ('online' mode) or in isolation from it ('offline' mode). In the tests described below, SES are performed offline with the LES data stored with the time interval Δt_{LES} , and filtering and interpolation done as a post-processing step.

4. Mean flow

The filtered LES field in the active region of the SES may have a non-zero mean velocity. Even in the case of the HIT, mean velocity over a chosen SES sub-region is non-zero instantaneously and of the order of U_{rms} . If such mean velocity becomes large, the residence time of the large-scale flow injected into the SES may not be long enough to allow the corresponding small-scale dynamics to develop. For instance, for the HIT, such mean residence time of the large-scale flow can be estimated as

$$\tau_{mf} = \frac{L_{SES}}{U_{rms}}, \quad (13)$$

where L_{SES} is the SES domain size. This can be compared with the characteristic turbulent eddy turnover timescale in the

SES domain

$$\tau_{ed,SES} = \frac{L_{SES}}{u_{\Delta}}, \quad (14)$$

where u_{Δ} is the characteristic velocity at the filter scale, Δ . The ratio of these two timescales would be

$$\frac{\tau_{mf}}{\tau_{ed,SES}} = \frac{u_{\Delta}}{U_{rms}} \sim \left(\frac{\Delta}{L_{LES}}\right)^{1/3}, \quad (15)$$

assuming Kolmogorov scaling, where L_{LES} is the LES domain size. In high- Re_{λ} flows, which are the primary target of the proposed approach, $\Delta \ll L_{LES}$, which could lead to very short residence times of the mean large-scale flow relative to the eddy turnover time in the SES, $\tau_{mf} \ll \tau_{ed,SES}$. In such cases, the mean velocity could be subtracted from the filtered LES data before calculating δu_i , i.e., eq. (1) can be modified as

$$\delta u_i = (\tilde{u}_{i,LES} - \overline{\tilde{u}_{i,LES}}) - \tilde{u}_{i,SES}, \quad (16)$$

where $\overline{\tilde{u}_{i,LES}}$ is the average filtered LES velocity in the SES domain. This can be interpreted as removing the zero-wavenumber component of the forcing LES velocity field, or alternatively it can be viewed as an SES domain, which is co-moving with the local LES flow in the Lagrangian framework.

In the tests discussed below, subtracting the mean velocity from the forcing flow did not affect the results since $\tau_{mf}/\tau_{ed,SES} \sim O(1)$, and all SES simulations presented below do not use this modification. Detailed analysis of the L/SES method performance in flows with large mean velocities is a subject of future work.

5. Summary of the L/SES algorithm

Finally, we summarize the sequence of algorithmic steps in the proposed L/SES approach described above:

1. Set up the large-scale simulation (LES), which resolves the large scales of the flow of interest, but does not capture the smallest scales of turbulence.
2. Select a sub-region of interest with size $\gtrsim 2\Delta$ within the LES domain for the SES calculation, where Δ is the filter scale chosen such that all scales $> \Delta$ are minimally affected by the lack of LES resolution or the subgrid-scale model uncertainties.
3. Set up a fully resolved SES grid in this sub-region. Also allocate an additional region around the SES domain for the sponge and buffer zones of size $\Delta/2$ and Δ , respectively.
4. Advance the LES calculation. Low-pass filter the LES fields at the filter scale Δ using eq. (4).
5. Perform spectral (or trigonometric) interpolation of the filtered LES data onto the SES grid, including the sponge and buffer regions, and a linear interpolation in time between the successive LES data snapshots.

6. Update the SES buffer with the interpolated LES data to specify the boundary conditions.
7. Inject the filtered and interpolated LES data into the SES simulation (only the active and sponge regions) at every time step using eq. (1) or (3).
8. Relax the SES solution to the LES field in the sponge region, according to eq. (8).
9. Advance the SES solution in time, and then repeat either from step 4 ('online' approach) or step 6 ('offline' approach).

III. ALTERNATIVE APPROACHES

A question can be asked whether other simpler approaches can achieve a similar goal as the L/SES method of embedding a high-fidelity local simulation in a lower-fidelity global model. Here we discuss two potential alternatives: one, which is similar to the traditional spectral forcing techniques, and one, which is based on the static (or adaptive) mesh refinement. In contrast to the L/SES, which combines both volumetric and boundary driving of the embedded simulation, approaches discussed here implement only one or the other type of driving. These two alternative methods also provide insights into the role of these two types of forcing and if both of them are essential to achieve high fidelity of the resulting solution.

A. Embedding of a high-resolution calculation through a scalar energy injection rate

Traditional methods of turbulence driving^{19,21,24,25} aim to inject energy into the simulation domain at a prescribed rate, ε . In a steady-state turbulence, this energy injection balances energy dissipation on small scales and allows an equilibrium cascade to establish. At the same time, for an arbitrary sub-region of interest in a larger system with an arbitrary flow, such rate of energy injection may differ from the global ε and it may not be immediately known. Furthermore, for a flow that is not in equilibrium, this rate of energy injection may be time-dependent and it may differ from the energy dissipation rate. In this section, we present a method where this energy injection rate into the chosen SES sub-region is determined on-the-fly from the LES using just the filtered fields of the large-scale flow, without making any assumptions of equilibrium. Resulting single scalar quantity, ε , is then used to force turbulence in the SES domain in a traditional way. This method can be viewed as a generalization of the traditional volumetric forcing approaches, including spectral¹⁹ and linear²⁵⁻²⁷ forcing.

The starting point is the same as in the L/SES approach described above. We choose a sub-region of interest of the LES calculation to be represented by an SES calculation with the domain size L_{SES} , as well as the scale, Δ_{ε} , at which energy would be injected. Considerations for the choice of Δ_{ε} are similar to the choice of the filter scale, Δ , in the L/SES

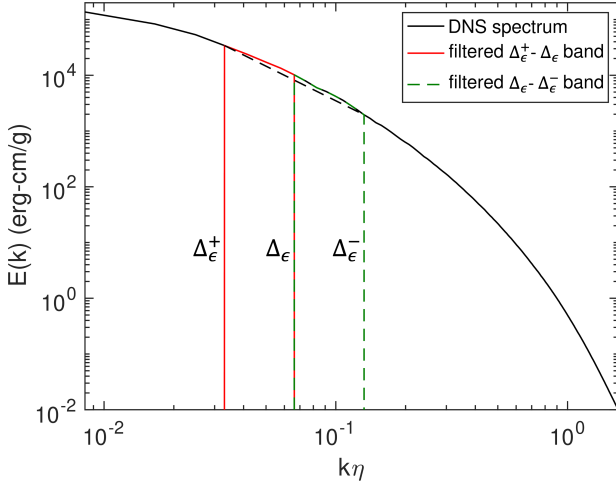


FIG. 7. Generic HIT spectrum illustrating the scale Δ_ε and the two bands used for the calculation of ε .

above. This scale should be contained within the SES, i.e., $\Delta_\varepsilon \leq L_{SES}$. For an explicitly filtered LES, Δ_ε could be chosen equal to the scale of explicit filtering, whereas for an implicitly filtered LES, it could be any scale that is minimally affected by numerical dissipation or SGS modelling of the LES. Here, we choose Δ_ε to be the largest scale available in the SES, i.e., $\Delta_\varepsilon = L_{SES}$.

For equilibrium turbulence, the specific kinetic energy spectral density takes the form $E(k) = C\varepsilon^{2/3}k^{-5/3}$, where k is the wavenumber and C is a constant. For a more general case of a non-equilibrium flow, the rate of energy transfer between different scales may be wavenumber-dependent, i.e., $\varepsilon = \varepsilon_0 k^x$. Then, spectral kinetic energy density at the scale Δ_ε can be written as

$$E(k_{\Delta_\varepsilon}) = C\varepsilon_0^{2/3}k_{\Delta_\varepsilon}^{2x/3-5/3} = Ak_{\Delta_\varepsilon}^{-\alpha}, \quad (17)$$

where $k_{\Delta_\varepsilon} = 2\pi/\Delta_\varepsilon$. Both A and α are unknown and time-dependent in the general case.

In order to determine ε at the scale Δ_ε , we consider two additional scales, one larger, Δ_ε^+ , and one smaller, Δ_ε^- , than Δ_ε (Fig. 7). We assume that the slope of $E(k)$ on a logarithmic scale between Δ_ε^+ and Δ_ε^- equals a constant $-\alpha$. This approximation of the local form of $E(k)$ is reasonable since the two scales Δ_ε^+ and Δ_ε^- can be chosen arbitrarily close to Δ_ε . We found that $\Delta_\varepsilon^+ = 2\Delta_\varepsilon$ and $\Delta_\varepsilon^- = \Delta_\varepsilon/2$ gave the best results.

From the original LES field, we find the band-pass filtered velocity field in the two bands Δ_ε^+ to Δ_ε and Δ_ε to Δ_ε^- , $u_{\Delta_\varepsilon^+}$ and $u_{\Delta_\varepsilon^-}$, respectively (Fig. 7). Band-pass filtering is achieved by applying a low-pass filter at each of the two scales and subtracting one result from the other. The filtering procedure is the same as described in § II A 1. Next, we calculate the r.m.s. of the resulting two band-pass filtered velocity fields $u_{\Delta_\varepsilon^+}$ and $u_{\Delta_\varepsilon^-}$. The r.m.s. is only taken over the sub-region corresponding to the SES domain.

The total specific kinetic energy in the two band-pass fil-

tered velocity fields can then be related to $E(k_{\Delta_\varepsilon})$ (eq. 17)

$$\frac{u_{\Delta_\varepsilon^+}^2}{2} = \int_{k_{\Delta_\varepsilon^+}}^{k_{\Delta_\varepsilon}} Ak^{-\alpha} dk = \frac{A}{\alpha-1} (k_{\Delta_\varepsilon^+}^{-\alpha+1} - k_{\Delta_\varepsilon}^{-\alpha+1}), \quad (18)$$

$$\frac{u_{\Delta_\varepsilon^-}^2}{2} = \int_{k_{\Delta_\varepsilon}}^{k_{\Delta_\varepsilon^-}} Ak^{-\alpha} dk = \frac{A}{\alpha-1} (k_{\Delta_\varepsilon}^{-\alpha+1} - k_{\Delta_\varepsilon^-}^{-\alpha+1}). \quad (19)$$

From these two equations, two unknowns α and A in eq. (17) can be found

$$\frac{u_{\Delta_\varepsilon^+}^2}{u_{\Delta_\varepsilon^-}^2} = \frac{k_{\Delta_\varepsilon^+}^{-\alpha+1} - k_{\Delta_\varepsilon}^{-\alpha+1}}{k_{\Delta_\varepsilon}^{-\alpha+1} - k_{\Delta_\varepsilon^-}^{-\alpha+1}} \implies \alpha = \alpha(u_{\Delta_\varepsilon^+}, u_{\Delta_\varepsilon^-}), \quad (20)$$

$$A = C\varepsilon_0^{2/3} = \frac{u_{\Delta_\varepsilon^-}^2}{2} \frac{\alpha-1}{(k_{\Delta_\varepsilon^+}^{-\alpha+1} - k_{\Delta_\varepsilon^-}^{-\alpha+1})}. \quad (21)$$

Equation (20) can be solved numerically to determine α . Substituting these constants into eq. (17), we finally determine the rate of energy injection in the SES domain

$$\varepsilon = \varepsilon_0 k^x = \left(\frac{A}{C}\right)^{3/2} k_{\Delta_\varepsilon}^{(5-3\alpha)/2}. \quad (22)$$

The constant $C \approx 1.5$ for HIT^{66,67}. Once ε is determined, it can subsequently be applied to force the SES simulation using any conventional volumetric forcing approach. Particular approach used in the tests below is described in § III A 1. We hereafter refer to this method as L/SES- ε .

L/SES- ε can be viewed as an extension of the traditional turbulence driving methods, in which ε actually represents the rate of the inter-scale kinetic energy transfer in a realistic flow instead of being an arbitrary parameter. Such energy transfer rate can be obtained directly without any assumptions regarding the nature of the flow, or the existence of equilibrium. As such, this method can be viewed as a test of the effectiveness of the traditional volumetric forcing methods in representing the effect of a large-scale ambient flow. Although proposed formulation extracts just a single scalar ε at the scale Δ_ε , this method can also be extended to implement anisotropic forcing by computing directional components of ε from the kinetic energy carried by the corresponding velocity components. At the same time, the key aspect is that in contrast to the L/SES approach, which injects the entire large-scale flow field into the SES, in the L/SES- ε approach, such large-scale flow is reduced to just a single scalar ε , which may not be sufficient to fully recover the corresponding structure of the small scales.

1. Spectral forcing with a given energy injection rate

A number of forcing strategies have been developed in the past^{19,27} for injecting kinetic energy volumetrically into the turbulent flow with a prescribed rate, ε (also see § I). Here we describe a spectral forcing approach^{20,49}, which can inject energy into the flow at a particular scale or over a range of scales. This forcing method is used both in the tests of L/SES- ε , as well as in the DNS described below.

First, we define velocity perturbations in spectral space as an independent realization of a Gaussian random field

$$\delta \hat{u}'_i(\mathbf{k}) = \sqrt{-2 \ln \phi_1} \cos(2\pi\phi_2) e^{i2\pi\phi_3}, \quad (23)$$

where ϕ_1 , ϕ_2 , and ϕ_3 are random variables uniformly distributed in the interval $(0, 1)$, \mathbf{k} is the wavenumber vector, u_i is the i^{th} component of the velocity, and \hat{u} represents a variable in the Fourier space.

Next, the function $\delta \mathcal{E}(k)$, which defines the spectral distribution of the energy injection rate, is prescribed as

$$\delta \mathcal{E}(k) = 1 \quad \forall \quad \frac{|k_i|}{2\pi/L} = 0, 1; \quad 0 \quad \text{otherwise.} \quad (24)$$

Here $k \equiv \|\mathbf{k}\|$ is the magnitude of the wavenumber. This particular form provides energy injection at the largest scale of the simulation domain, although in general the function $\delta \mathcal{E}(k)$ can be arbitrarily complex, and it can support broadband energy injection. This energy injection spectrum is applied to the velocity perturbation field as

$$\delta \hat{u}'_i(\mathbf{k}) = \frac{\sqrt{\delta \mathcal{E}(k)}}{k} \delta \hat{u}''_i(\mathbf{k}). \quad (25)$$

To ensure that the perturbations are solenoidal in physical space, an orthogonal projection is taken

$$\delta \hat{u}_i(\mathbf{k}) = \left(\delta_{ij} - \frac{k_i k_j}{k^2} \right) \delta \hat{u}'_j(\mathbf{k}), \quad (26)$$

where δ_{ij} is the Kronecker delta. Resulting perturbations are then transformed to the physical space and normalized to provide the prescribed energy injection rate ε . The total momentum of the perturbations is subtracted to ensure that no net momentum is introduced. Finally, resulting velocity perturbation field is directly added to the velocity field at each time step

$$u_i^{n+1} = u_i^n + \delta u_i. \quad (27)$$

B. Embedding of a high-resolution region through mesh refinement

Both L/SES and L/SES- ε methods described above require two separate simulations LES and SES, running sequentially or concurrently, as well as explicit filtering of the velocity fields. Therefore, a question can be asked whether these approaches can be replaced with a simple mesh refinement, which can be embedded inside an LES sub-region of interest and which would not require any elaborate forcing mechanisms³⁶⁻³⁹. In this approach, such sub-region is statically or adaptively refined to resolve the full range of small scales. Figure 8 shows such statically refined mesh in a periodic cube containing HIT. Each block represents 16^3 cells. The central high-resolution region is surrounded by progressively coarser cells to limit the refinement factor to 2 between adjacent mesh blocks. This proper nesting requirement is typical for the modern mesh refinement algorithms⁶⁸⁻⁷⁰, and it is in agreement with the prior analysis by others^{38,39}.

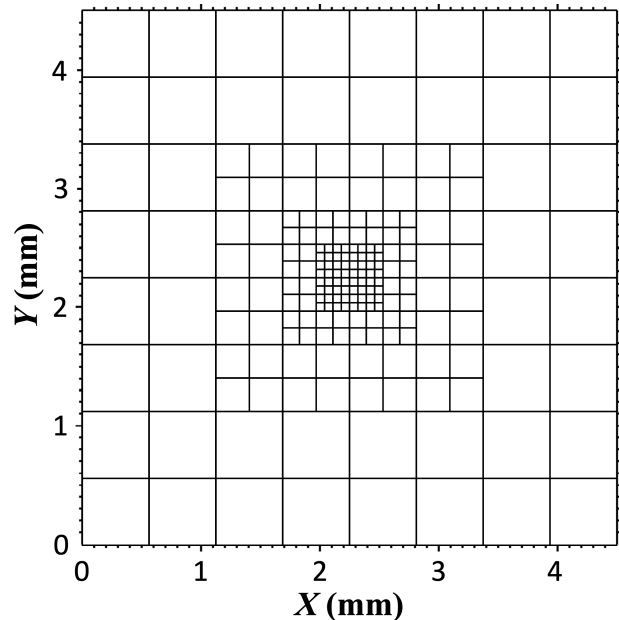


FIG. 8. Grid structure in the midplane of the SMR calculations. Each block represents 16^3 computational cells.

Static (SMR) and adaptive (AMR) mesh refinement are well established computational techniques, which have been used over the years in a wide range of problems from engineering⁷¹⁻⁷³ to astrophysics⁷⁴. Traditionally, proper use of SMR or AMR assumes that the entire flow feature of interest, such as a shock wave, a flame, or a shear layer are fully resolved. This ensures that such features do not cross the coarse-fine grid boundaries, which are prone to introduce errors in the solution. This particularly concerns regions with turbulence, which typically are expected to be captured with uniform resolution. Therefore, proposal to refine only a sub-region of a turbulent flow, as in Fig. 8, is contrary to the established practices for the use of SMR/AMR. Nevertheless, we investigate here whether such selective refinement of a turbulent flow can yield positive results, which could obviate the need for more complex methods, such as L/SES or L/SES- ε .

Finally, in contrast to the L/SES- ε strategy described above, which implements purely volumetric forcing, this approach that we refer to as L/SES-SMR, effectively represents only boundary forcing. The large-scale flow structures enter the high-resolution region through the coarse-fine boundaries. Thus, the detailed treatment of such boundaries is central to this method. Any artifacts associated with flux interpolation at the coarse-fine boundaries, or any other aspects of the numerical algorithm, will be advected into the region of interest, where they can affect the small-scale flow structure that has to develop there. Detailed tests of both the L/SES- ε and L/SES-SMR approaches, and their comparison with the performance of the L/SES method, are described below.

	e-HIT DNS	ne-HIT DNS
Domain width, L_{DNS} (cm)	0.45	0.9
Grid size	1024 ³	1024 ³
Energy injection rate, ε (erg/g s)	5.29×10^9	3.43×10^9
Density, ρ (g/cm ³)	1.10×10^{-3}	8.73×10^{-4}
Kinematic viscosity, ν (cm ² /s)	0.15	0.19

TABLE I. Parameters of the DNS.

IV. NUMERICAL MODEL AND SIMULATION SETUP

All methods described above solve the Navier-Stokes equations

$$\frac{\partial \rho}{\partial t} + \frac{\partial \rho u_j}{\partial x_j} = 0, \quad (28)$$

$$\frac{\partial \rho u_i}{\partial t} + \frac{\partial \rho u_i u_j}{\partial x_j} = -\frac{\partial p}{\partial x_i} + \frac{\partial \sigma_{ij}}{\partial x_j} + f_i, \quad (29)$$

$$\frac{\partial \rho E}{\partial t} + \frac{\partial (\rho E + p) u_j}{\partial x_j} = \frac{\partial}{\partial x_j} \left(\kappa \frac{\partial T}{\partial x_j} \right) + \frac{\partial u_i \sigma_{ij}}{\partial x_j} + u_j f_j, \quad (30)$$

where u_i is the fluid velocity, ρ is the density, $p = (\gamma - 1)\rho e$ is the pressure, $E = e + u_j u_j / 2$ is the total energy per unit mass, e is the internal energy per unit mass, γ is the specific heat ratio set to a constant value of 1.197 in all tests described below, $\sigma_{ij} = 2\mu S_{ij} - 2/3\mu S_{kk}\delta_{ij}$ is the viscous stress tensor with the strain rate $S_{ij} = \frac{1}{2}(\frac{\partial u_i}{\partial x_j} + \frac{\partial u_j}{\partial x_i})$, δ_{ij} is the Kronecker delta, $\mu = \rho\nu$ is the coefficient of viscosity, ν is the kinematic viscosity, T is the temperature, and $\kappa = 6.234 \times 10^3$ erg/(s cm K) is the thermal conductivity.

Additional terms f_i and $u_i f_i$ represent external forcing, which takes on different meaning depending on the calculation. In particular, forcing described by these terms in the DNS and in the SES- ε tests is detailed in § III A 1 above. In the SES, the forcing procedure is described in § II. Finally, the details of forcing in the SES-SMR tests is given in § IV C below.

All simulations, with the exception of the SES-SMR, are performed using a fully compressible, massively parallel, numerical solver Athena-RFX⁴⁹, a reacting-flow extension of the code Athena⁷⁵. The code uses a higher-order, fully conservative, Godunov-type method for integration based on the unsplit corner transport upwind (CTU) algorithm^{50,51}. The integration scheme uses piecewise parabolic method (PPM) for spatial reconstruction⁵², along with an approximate non-linear Harten-Lax-van Leer contact (HLLC) Riemann solver. The overall scheme is 3rd-order accurate in space and 2nd-order accurate in time. Further details of the algorithm and its implementation can be found in Gardiner and Stone⁷⁶ and Stone *et al.*⁷⁵, while the detailed tests of the code for modeling the HIT are described in Hamlington, Poludnenko, and Oran^{77,78}. The code has been extensively used in a wide variety of reacting and non-reacting flow studies^{5,49,77-81} in-

cluding detonations⁸²⁻⁸⁴. All calculations performed with Athena-RFX use a uniform, Cartesian grid.

The SES-SMR calculations were performed with the code Athena-RFX++, a reacting flow extension of the code Athena++, which implements both static and adaptive mesh refinement on a block-structured grid⁸⁵. This code also implements a range of higher-order, Godunov-type integrators, including the van Leer predictor-corrector scheme used in this work⁸⁶. Spatial reconstruction and the Riemann solver are the same as in Athena-RFX, giving the same order of accuracy of the overall algorithm. Resulting turbulent flow fields obtained with both codes were verified to be statistically identical.

A. Direct numerical simulations for the *a priori* tests

In the present work, we restrict ourselves to the *a priori* tests of the method, in which no LES are directly performed. Instead, a fully resolved DNS is explicitly filtered at an appropriate scale (in the inertial range) to mimic the LES field and obtain the forcing data for the SES. The *a priori* approach is chosen here for two reasons. First, we seek to demonstrate that the L/SES method can work in principle for physically correct large-scale flows not affected by the numerics or the subgrid-scale models. Second, DNS also provides the reference small-scale flow structure for direct comparison with that obtained in the SES. This is in contrast with the *a posteriori* tests based on the LES, for which results can be compared with the DNS only statistically. Such statistical comparison is not sufficient in the case of unsteady flows. Detailed *a posteriori* tests for a range of Re_λ values will be presented in the follow-up paper.

Two reference DNS of the HIT are performed by solving eqs. (28) - (30) in a cubic, triply periodic domain on a 1024³ grid. Parameters of both DNS are given in Table I. The first DNS considers driven equilibrium HIT in a steady state and is hereafter referred to as the e-HIT DNS. Turbulence in this simulation is stirred at the scale of the domain width, L_{DNS} , using the approach described in § III A 1. The calculation is initialized with uniform density $\rho = 1.104 \times 10^{-3}$ g/cm³ and atmospheric pressure. The initial velocity field in the domain is prescribed with the kinetic energy spectrum given by the power-law of the form $E(k) \propto k^{-5/3}$. To reach an equilibrium, the flow is allowed to develop for two large-scale eddy turnover times, τ_{ed} ,

$$\tau_{ed} = \frac{L_{DNS}}{U_{L,DNS}}. \quad (31)$$

Here $U_{L,DNS}$ is the velocity at the scale L_{DNS} . We note that τ_{ed} is approximately four times larger than the integral-scale eddy turnover time⁴⁹. After the initial equilibration period, the e-HIT DNS is continued for another $2\tau_{ed}$ to provide forcing data and collect the statistics for evaluating the performance of the companion SES.

Since we seek to devise a general method, which is agnostic to the underlying flow conditions, the e-HIT DNS is supplemented with the second reference DNS that we use to study

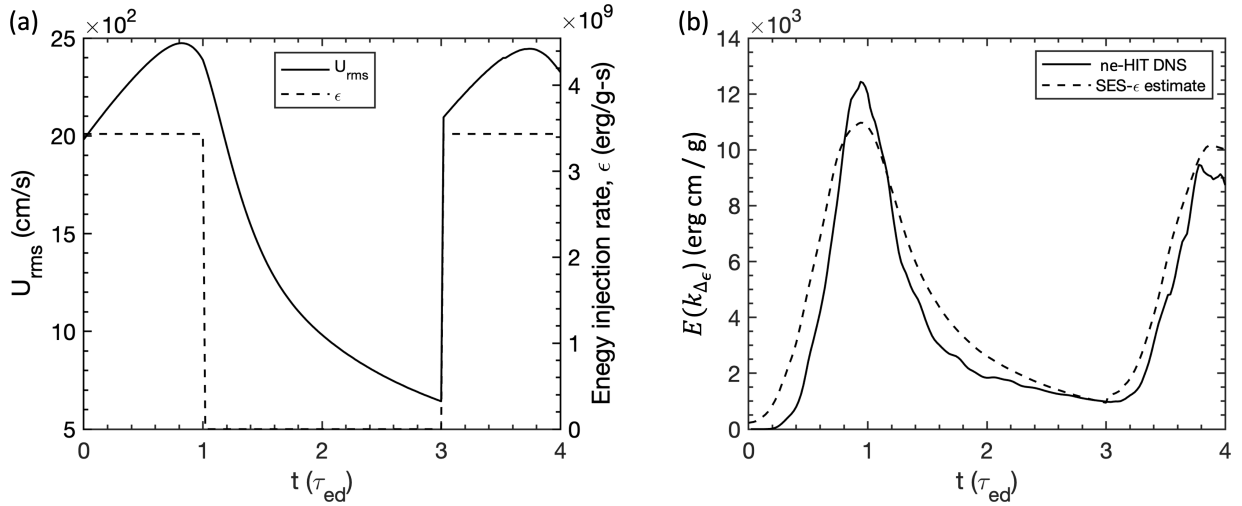


FIG. 9. a) The U_{rms} and the energy injection rate ϵ as a function of time in the ne-HIT DNS. b) Spectral kinetic energy density at the scale Δ_ϵ in the ne-HIT DNS obtained directly from the spectrum (solid line) and using the SES- ϵ approach (§ III A) (dashed line).

the time-dependent performance of the proposed L/SES approach in turbulent flows out of equilibrium. This unsteady DNS, hereafter referred to as ne-HIT, is initialized in the same way as the e-HIT DNS with the parameters given in Table I. For the first τ_{ed} , the simulation is forced with a constant ϵ using the same method as in the e-HIT DNS. Driving is then stopped, and turbulence is allowed to decay for the next $2\tau_{ed}$. Note that during this time, the actual τ_{ed} would be changing, however hereafter we use the equilibrium steady-state value of τ_{ed} to specify time intervals both in the ne-HIT DNS and the companion SES. At $3\tau_{ed}$, driving is restarted by injecting at the largest scale the amount of energy needed to increase the r.m.s. velocity in the domain, U_{rms} , to the value close to that at $t = 0$. After that, forcing is continued for another τ_{ed} with the original energy injection rate ϵ . This progression is illustrated in Fig. 9a, which shows both ϵ and U_{rms} in the ne-HIT DNS as a function of time. As a result, ne-HIT DNS consists of periods of turbulence growth, decay, and sudden increase of energy injection creating strong turbulent non-equilibrium. Thus, this case allows us to test the L/SES approach under more complex turbulent flow conditions compared to the more idealized, steady, equilibrium HIT.

In both DNS calculations, grid resolution was chosen to provide at least two cells per Kolmogorov scale (see Table III). Such resolution was previously found sufficient to ensure high fidelity of the DNS solution^{53–55}. Resulting turbulence in both DNS has a very low degree of compressibility with the r.m.s. Mach number ≈ 0.05 .

Finally, we note that these two calculations do not represent DNS of some realistic flow due to the presence of artificial large-scale forcing. For the purposes of this work, however, we use these two calculations to provide: i) the canonical, well established reference flow with a sufficiently high Re_λ , ii) a realistic large-scale turbulent flow of sufficient complexity for SES forcing, and iii) a fully resolved reference small-scale flow for direct comparison with the SES.

B. SES and SES- ϵ tests

Companion SES and SES- ϵ tests are set up and driven with the flow fields obtained in the e-HIT and ne-HIT DNS using methods described in § II and III A. All SES tests were performed in the ‘offline’ mode, i.e., separately from the DNS, using large-scale forcing data recorded and stored at discrete time intervals $\Delta t_{forcing} \approx 0.36\Delta/U_{rms}$ for the e-HIT DNS and $\approx 0.64\Delta/U_{rms}$ for the ne-HIT DNS in agreement with the criterion given in eq. (10) (see § II A 3).

For the e-HIT SES- ϵ test, ϵ obtained from the e-HIT DNS was time-averaged and the resulting value was used as a constant energy injection rate for the entire calculation. This time-averaged value was found to be 3.92×10^9 erg/g·s vs. the actual $\epsilon = 5.29 \times 10^9$ erg/g·s in the e-HIT DNS (Table I), or 26% lower.

For the ne-HIT SES- ϵ , Fig. 9b shows the time-dependent spectral density of the specific kinetic energy at the filter scale $\Delta_\epsilon = L_{SES}$, or $E(k_{\Delta_\epsilon})$. Values obtained directly from the kinetic energy spectra at this scale in the ne-HIT DNS are shown with a solid black line, while the dashed line shows values calculated using eq. (17) with A and α found following the procedure in § III A (eqs. 20, 21). These A and α are then used to calculate ϵ based on eq. (22). Close agreement of the $E(k_{\Delta_\epsilon})$ obtained using the SES- ϵ approach with the exact DNS values demonstrates that both A and α , and thus ϵ derived from them and used to force the SES- ϵ calculation, accurately capture the complex flow evolution in the ne-HIT DNS.

The central cubic sub-region of the DNS domain was chosen as the region of interest for the SES tests. In both SES cases, the filter scale $\Delta = 64dx_{DNS}$, and the size of the active region of the domain is set to $L_{SES} = 2\Delta$ as discussed in § II A. For SES- ϵ , $\Delta_\epsilon = L_{SES} = 128dx_{DNS}$. Both the grid size and L_{SES} for the SES and SES- ϵ tests are given in Table II. The choice of the location of the sub-region is arbitrary and any other sub-region could be considered instead. Grid cell size in the SES and SES- ϵ is equal to that in the corresponding DNS.

	e-HIT SES	e-HIT SES- ϵ	ne-HIT SES	ne-HIT SES- ϵ
L_{SES} (cm)	0.05625	0.05625	0.1125	0.1125
Sponge size (cm)	0.0140625	—	0.028125	—
Grid size	$(128 + 64)^3$	128^3	$(128 + 64)^3$	128^3

TABLE II. Parameters of the SES and SES- ϵ . For the SES, grid size in parenthesis includes both the active and sponge regions.

Initial conditions in the SES were set directly based on the full flow field in the central region of the corresponding DNS at $t = 0$. Boundary conditions were also set directly from the DNS field as described in § II A 2. In contrast, SES- ϵ tests were run with periodic boundaries. They were initialized with the same constant density and pressure as the corresponding DNS. Initial velocity field was set with the same spectral kinetic energy distribution of the corresponding DNS.

C. SES-SMR tests

The L/SES-SMR approach does not admit *a priori* testing since most of the flow in the domain is by design unresolved. Nevertheless, we include the tests of this method since it is considerably simpler algorithmically than the L/SES and L/SES- ϵ approaches, as it can be implemented effectively using any existing SMR/AMR code. Thus it is important to understand whether it can potentially provide a more cost-effective alternative to L/SES and L/SES- ϵ .

Tests of the L/SES-SMR (§ III B) consider only equilibrium, steady-state HIT in a 3D periodic cube, and thus they are similar in setup to the e-HIT DNS. In particular, SES-SMR tests have the same domain size and other parameters of the e-HIT DNS listed in Table I. The only difference is the non-uniform computational grid shown in Fig. 8. The central high-resolution region has the same physical size L_{SES} , grid size equal to 128^3 , and the computational cell size as the SES (excluding sponge regions) and SES- ϵ tests. Outside this central region, resolution gradually decreases by a factor of two over the next 3 levels of refinement. The coarsest region has the resolution equivalent to that of the 128^3 grid. Note that even though the coarse regions of these simulations are not well-resolved, eqs. (28) - (30) are directly evolved in the non-uniform grid without using any closure models.

Turbulence is forced with the prescribed rate ϵ at the scale of the domain width using the same spectral forcing approach outlined in § III A 1 as in the e-HIT DNS. At the same time, presence of a non-uniform mesh prevents the forcing method from being applied in its standard form. Instead, we consider three modifications of forcing.

In the first one, velocity perturbation field δu_i is first formed in exactly the same way as in the e-HIT DNS on a uniform $1,024^3$ mesh spanning the entire computational domain (Fig. 8). Subsequently, δu_i are applied as is in the fine central region. In the coarser outer cells, δu_i are averaged over the corresponding finer cells of the source uniform mesh before being applied to the velocity field using eq. (27). We refer to this test as SES-SMR1.

This approach, however, is somewhat artificial as it pre-

sumes that the effect of large scales is known in the central region of interest, and thus it injects the large-scale flow information into the central region volumetrically, and not just through the region boundaries. In a practical LES simulation, no such large-scale forcing would be present as the large-scale flow dynamics would directly emerge in the process of flow evolution. Therefore, another test, SES-SMR2, is performed, in which exactly the same velocity perturbation field δu_i is applied everywhere except for the most-refined central region, i.e., in that region δu_i are set to zero. This approach produces the same flow field outside the central region, where it maintains the same rate of kinetic energy injection per unit volume as in SES-SMR1, however the total amount of injected energy in the domain is reduced.

Finally, the third test, SES-SMR3, is performed, in which similar to SES-SMR2 no energy is injected in the most refined region. Instead, volumetric energy injection rate in the outer regions is increased to ensure that the total rate of energy injection in the domain is the same as in the first SES-SMR1 case. Together, these three cases span the range of possibilities for forcing an embedded SMR simulation, and thus they allow us to elucidate the difference in the solution accuracy achievable through SMR vs. L/SES.

V. RESULTS

Figure 10a shows the instantaneous flow structure, in particular vorticity magnitude in the midplane of the computational domain, in the fully developed e-HIT DNS. Central region chosen for the SES is marked with a dashed black line. Magnified view of this central region is given in Fig. 10b. Corresponding flow fields in the SES and SES- ϵ at the same time instant are shown in Figs. 10c and 10d, respectively. Forcing of the two SES was performed using the instantaneous DNS velocity fields, as described in §§ II and III.

Qualitatively, the flow in the SES calculation appears to be virtually indistinguishable from the corresponding region in the full DNS. At the same time, in the SES- ϵ calculation, not only is the flow structure completely different, but more importantly the vorticity magnitude is considerably lower. We quantify this observation below using U_{rms} . We do not show here the instantaneous flow structure in the SES-SMR calculations since they are not correlated with the DNS.

A. Global characteristics of turbulence

While the qualitative comparison of the flow structure suggests that the SES calculation, unlike SES- ϵ , is able to cap-

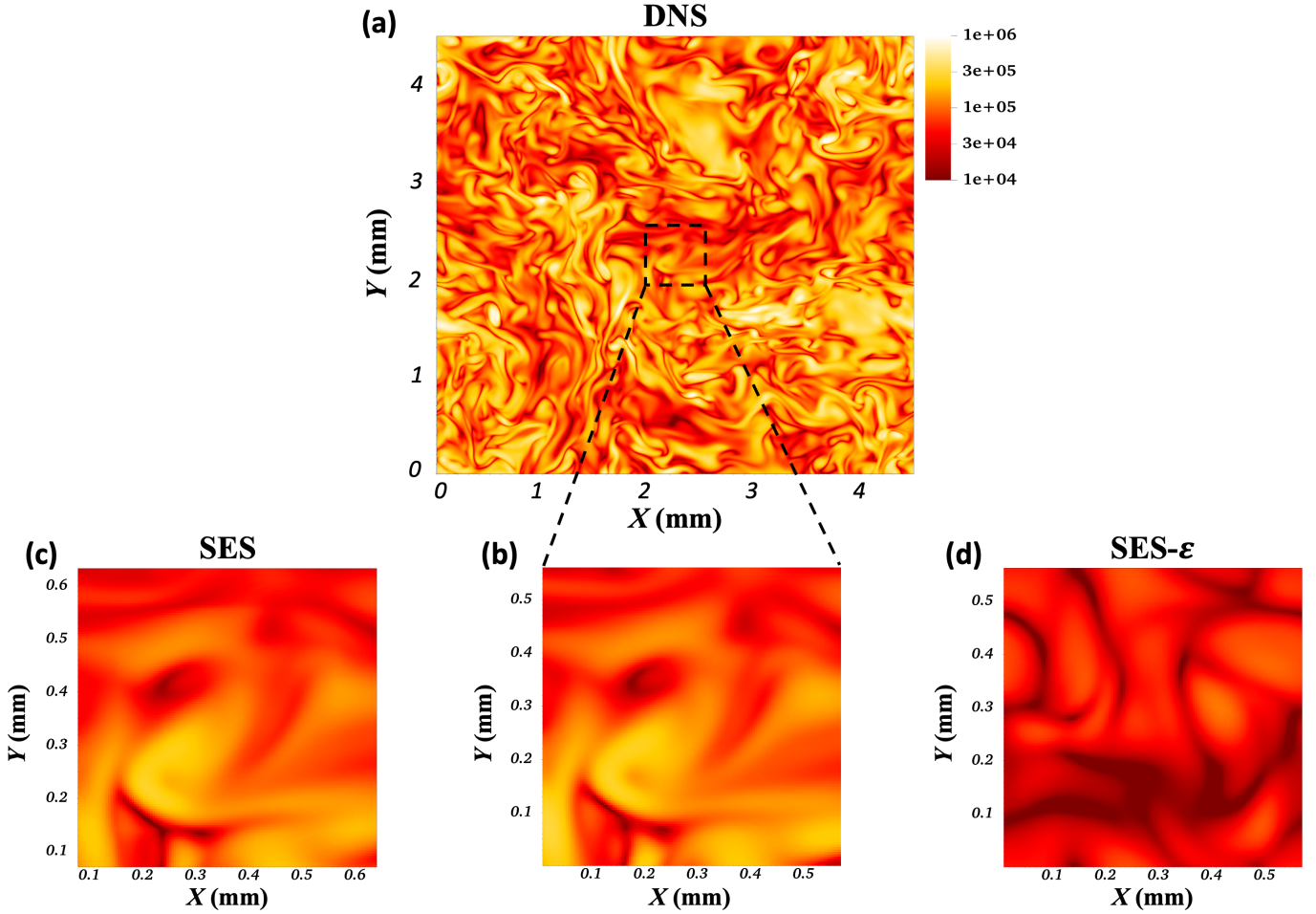


FIG. 10. Vorticity magnitude field at a representative time instant in the e-HIT simulations. (a) Full DNS, (b) magnified view of the central sub-region of the DNS, (c) SES, and (d) SES- ϵ .

ture in detail the small-scale flow in the region of interest in the DNS, it is important to consider more quantitative metrics of the solution accuracy. First, we compare global turbulence characteristics, such as kinetic energy in the domain in terms of U_{rms} , Taylor scale λ and the associated Reynolds number Re_λ , and the average Kolmogorov scale, η . For the equilibrium turbulence calculations, all statistics are averaged in time over 267 samples during the final $2\tau_{ed}$. For ne-HIT, statistics are considered with respect to time with all data being collected every 9.8×10^{-6} s, or $0.02\tau_{ed}$, from the start of the simulation.

Key turbulence properties obtained in all e-HIT SES tests are listed in Table III, along with the values in the corresponding central region of the e-HIT DNS for comparison. In all calculations, turbulence is well resolved^{53–55} with the Kolmogorov scale

$$\eta = \left(\frac{v^3}{\langle \epsilon' \rangle} \right)^{1/4} \approx 2\Delta x. \quad (32)$$

Here, Δx is the computational cell size, $\epsilon' = 2\nu S_{ij}S_{ij}$ is the dissipation (different from the energy injection rate ϵ), S_{ij} is the strain rate, and $\langle \epsilon' \rangle$ indicates averaging over space and

	\bar{U}_{rms} (cm/s)	Re_λ	$\eta/\Delta x$	λ/η
DNS	1797.3	145.6	2.04	23.75
SES	1681.5	114.2	1.91	20.75
SES- ϵ	850.44	51.6	2.02	11.13
SES-SMR1	1454.1	88.3	1.84	18.72
SES-SMR2	1323.6	59.6	1.98	15.36
SES-SMR3	1422.2	78.7	1.85	17.24

TABLE III. Turbulence properties in the DNS and SES calculations.

time.

The total amount of kinetic energy represented by the time-averaged \bar{U}_{rms} shows a wide spread among different tests. SES gives by far the best agreement with the DNS, with \bar{U}_{rms} being within 6.4% of the DNS value. In contrast, in the SES- ϵ , \bar{U}_{rms} is more than a factor of two smaller. Finally, for all three SES-SMR tests (see § IV C), the agreement is worse than in SES but substantially better than for SES- ϵ with the deficit relative to DNS ranging from 19% to 26%. Note that such large deficit in total kinetic energy is observed regardless of whether the volumetric forcing is applied in the central high-

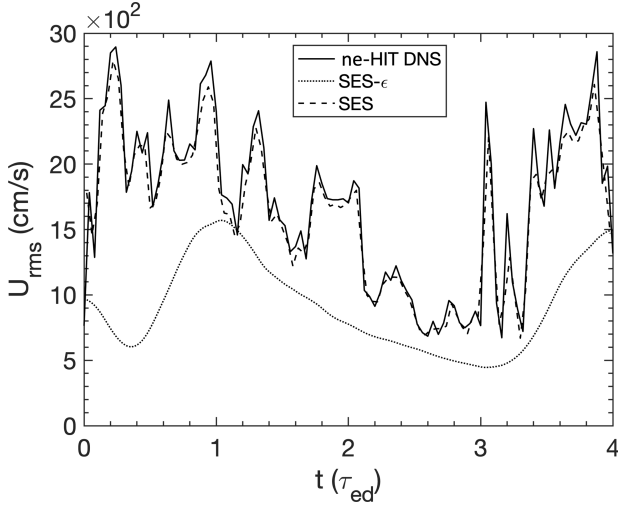


FIG. 11. Evolution of the r.m.s. velocity in the ne-HIT DNS, SES, and SES- ϵ . DNS values are considered over the central region only.

resolution region (SES-SMR1 test), and also even when the total rate of kinetic energy injection in the domain is the same as in the DNS (SES-SMR1 and SES-SMR3 tests).

Similar trends are also observed for the turbulent Taylor scale

$$\lambda = \frac{\langle u_j u_j \rangle^{1/2}}{\langle (\partial u_i / \partial x_i)^2 \rangle^{1/2}}, \quad (33)$$

and the associated Taylor-scale Reynolds number

$$\text{Re}_\lambda = \frac{U_l \lambda}{\nu}, \quad (34)$$

in the e-HIT calculations shown in Table III. Here, $\langle \dots \rangle$ again indicates space and time averaging, $U_l = U_{rms} / \sqrt{3}$ is the integral velocity, and kinematic viscosity ν is given in Table I. In particular, while in the SES, Re_λ is within 22% of the DNS value, it is almost a factor of 3 too low in SES- ϵ , and between 40% to more than a factor of 2 too low for the SES-SMR tests. Similar level of agreement is also seen for the ratio λ / η .

Figure 11 shows U_{rms} in the unsteady ne-HIT DNS, SES, and SES- ϵ . In the SES, U_{rms} (dashed line) tracks the DNS (solid line) very closely through all stages of the flow evolution including both forced equilibrium and non-equilibrium turbulence, as well as decaying turbulence.

In contrast, while U_{rms} in SES- ϵ (dotted line in Fig. 11) is generally correlated with the ne-HIT DNS on larger timescales and it captures all the transient phases of the flow, the actual values of U_{rms} are again substantially lower. Thus, $L/\text{SES-}\epsilon$, which relies only on the large-scale energy transfer rate in the cascade, significantly underpredicts kinetic energy in the region of interest both in the e-HIT and ne-HIT, thereby also leading to much lower Reynolds numbers compared to the host flow (cf. Table III).

This disagreement cannot be attributed solely to the underprediction of ϵ by the SES- ϵ procedure (§ III A). For instance, it was stated in § IV B that ϵ in the e-HIT SES- ϵ is $\approx 26\%$

lower than in the corresponding DNS. This, however, would reduce U_{rms} by only 10% based on the Kolmogorov scaling, and thus this difference in ϵ would not explain the fact that U_{rms} in SES- ϵ is twice lower than in the e-HIT DNS. Instead, the cause of much lower kinetic energy in the SES- ϵ is the fact that in this approach, turbulent velocities at the largest scale L_{SES} in the domain are comparable to the velocities at the same scale in the DNS, but much smaller than the velocities at the largest scale of the DNS $L_{DNS} \gg L_{SES}$. As a result, kinetic energy in the domain, and thus λ and Re_λ , are significantly under-predicted compared to the DNS. This is confirmed if we compare the ratio of U_{rms} in the SES- ϵ and DNS with the inertial range scaling law⁷

$$\frac{U_{rms,SES-\epsilon}}{U_{rms,DNS}} = 0.47 \approx \left(\frac{L_{SES}}{L_{DNS}} \right)^{1/3} = 0.50. \quad (35)$$

In contrast, L/SES does not suffer from this deficiency. While not capturing the large scales explicitly, the SES domain nevertheless contains the velocities associated with the large-scale motions since they are directly introduced into the SES domain via the forcing procedure. As a result, the L/SES method can generate turbulence with global characteristics very close to a full-scale simulation both in the steady-state and unsteady turbulence despite having a much smaller dynamical range of scales available in the domain.

B. Kinetic energy spectra

Next, we compare the spectral distribution of kinetic energy density in all calculations. In the periodic DNS and SES- ϵ domains, 1D kinetic energy spectrum is calculated in the usual way. For the DNS, spectrum is taken over the entire domain to show the energy content at all wavenumbers.

At the same time, since SES uses a non-periodic domain, while SES-SMR has a non-periodic, high-resolution central region of interest, care must be taken obtaining the corresponding turbulent spectra. To minimize the aliasing errors, we use a Hann window function of the form

$$w = \cos^2\left(\frac{\pi x}{L_x}\right) \cos^2\left(\frac{\pi y}{L_y}\right) \cos^2\left(\frac{\pi z}{L_z}\right). \quad (36)$$

Here, x, y, z are the cell-center coordinates relative to the center of the domain, and $L_x = L_y = L_z = L_{SES}$.

Resulting spectrum of the windowed field needs to be appropriately re-scaled to compensate for the reduction in the energy caused by the windowing operation and thus to ensure that the windowed field has the same energy as the original field. The exact correction factor is signal dependent. Since the velocity-field signal can be considered stationary in space due to the flow homogeneity, the correction factor can be estimated as the inverse of the r.m.s. of the window function, w_{rms} . For the Hann window in 1D,

$$w_{rms} = \left(\frac{1}{L_x} \int_{-L_x/2}^{L_x/2} \cos^4\left(\frac{\pi x}{L_x}\right) dx \right)^{1/2} = \frac{3}{8}. \quad (37)$$

Thus, the kinetic energy spectral density of the windowed velocity field must be scaled by the factor $((8/3)^3)^2$.

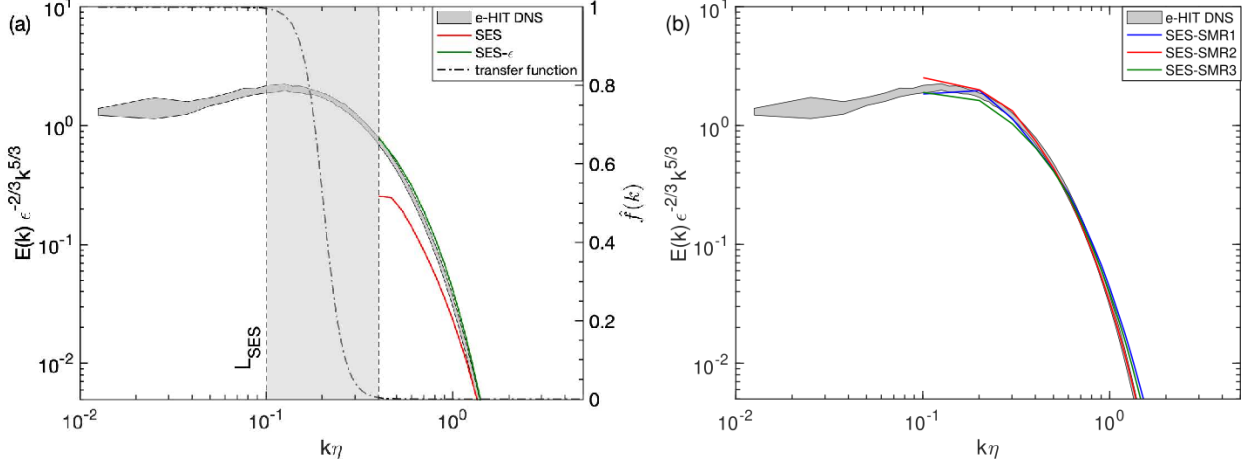


FIG. 12. Time-averaged kinetic energy spectra in the e-HIT SES and SES- ε calculations (panel a) and the e-HIT SES-SMR tests (panel b). Both panels show the range of spectra variability in the e-HIT DNS (gray band). All spectra are compensated by the Kolmogorov scaling. In panel (a), scales affected by filtering are marked as a vertical gray region, and SES spectra are not shown in this range. Transfer function of the filter is shown on the right axis of panel (a).

Finally, another correction must be introduced in the SES and SES-SMR spectra to account for the fact that velocities associated with scales larger than L_{SES} are present in the SES domain. Such large-scale motions cannot be properly represented in the spectrum, which does not contain scales $> L_{SES}$. At the same time, energy associated with such motions is distributed among the available scales in the SES spectrum since the total kinetic energy in the SES domain and in the spectrum must be equal to satisfy the Parseval's theorem (also cf. U_{rms} in Table III). This leads to a higher spectral kinetic energy density in the SES. To correct for this, another scaling factor is applied, which represents the ratio of the energy on small scales $< L_{SES}$ to the total specific kinetic energy in the SES

$$\frac{E^{SS}}{E} = \frac{U_{rms}^2 - \tilde{U}_{rms}^2}{U_{rms}^2}. \quad (38)$$

Here, U_{rms} and \tilde{U}_{rms} are the r.m.s. of the raw and filtered velocity field respectively, with filtering applied at the scale of the SES active domain size L_{SES} , and SS represents scales smaller than this cutoff. Therefore, finally, all SES and SES-SMR spectra are normalized by the factor $(E^{SS}/E)/w_{RMS}^6$.

Figure 12a shows the time-averaged, compensated energy spectra in the e-HIT SES and SES- ε , along with the range of variability of the spectra in the DNS. SES- ε spectra agree closely with the DNS, which is expected since SES- ε obtains ε directly from the DNS, and it is forced in the same way as the DNS. For the SES, agreement with the DNS is slightly worse, in particular at scales close to the filter scale, Δ . This is the result of these scales being affected by the large-scale flow-field injection. At sufficiently high Re_λ , the impact on small scales that one is interested in should be minimal. Note that limited spectral sharpness of the filter affects scales close to the filter size Δ (see § II A 1). Therefore, scales in the range $[\Delta/2, 2\Delta]$, represented by the vertical gray region, were

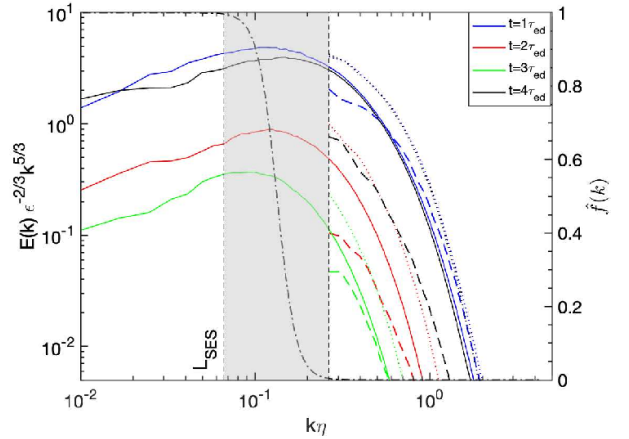


FIG. 13. Kinetic energy spectra at a few representative time instants (cf. Fig. 9) in the ne-HIT SES and SES- ε calculations (see text for further details). Solid lines: ne-HIT DNS, dashed lines: SES, dotted lines: SES- ε . All spectra are compensated by the Kolmogorov scaling. Scales affected by filtering are marked as a vertical gray region, and SES spectra are not shown in this range. Transfer function of the filter (dash-dot line) is shown on the right axis.

removed from the SES spectra in both panels. Similar comparison of the time-averaged spectra for the SES-SMR tests, is shown in Fig. 12b. Close agreement with the DNS, similar to that for SES- ε , can be seen.

Evolution of spectra in the unsteady ne-HIT case is illustrated in Fig. 13, which shows the instantaneous compensated spectra in the SES and SES- ε calculations at several representative time instants. These correspond to the end of the forcing stage when turbulence becomes fully developed ($t = \tau_{ed}$), middle of the decaying turbulence phase ($t = 2\tau_{ed}$), time when forcing is restarted ($t = 3\tau_{ed}$), and end of the simulation when

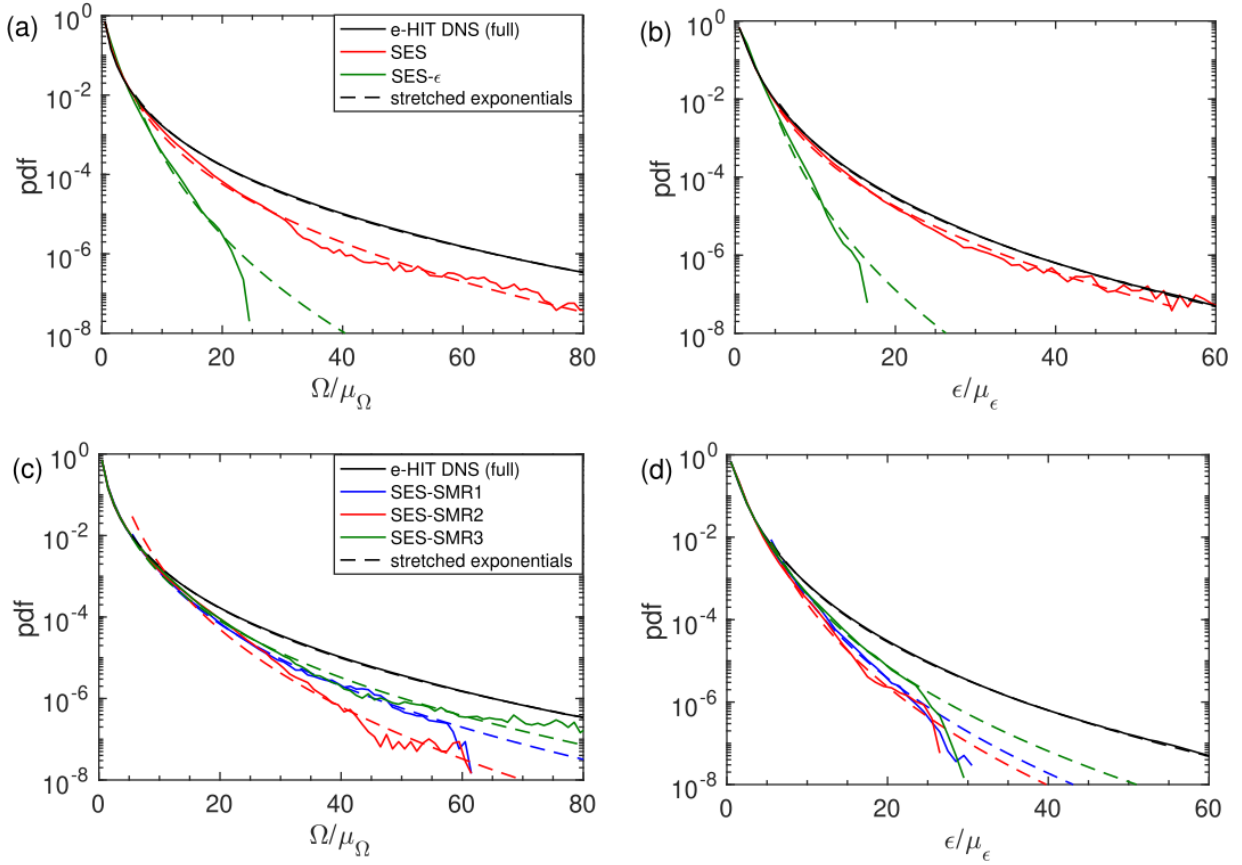


FIG. 14. Time-averaged PDF of enstrophy, Ω (a, c), and dissipation rate, ϵ (b, d), for the e-HIT DNS (full domain), SES and SES- ϵ (a, b), and SES-SMR (c, d). Dashed lines show the stretched exponential fits.

turbulence again re-equilibrated ($t = 4\tau_{ed}$) (cf. Fig. 9). Again, similar to Fig. 12, scales affected by the filter are excluded. For the SES- ϵ (dotted lines), agreement with the DNS (solid lines) is worse than in the e-HIT case, however, the SES- ϵ is able to follow the overall spectral evolution over different stages. For the SES (dashed lines), agreement with the DNS is comparable to or better than for the SES- ϵ , with the exception of $t = 4\tau_{ed}$, where the SES spectrum deviates more strongly from the DNS.

C. Small-scale intermittency

While turbulent velocities in the HIT are Gaussian⁸⁷, velocity gradients and the associated small-scale quantities, such as enstrophy, $\Omega = \omega_i \omega_i / 2$, where $\boldsymbol{\omega} = \nabla \times \mathbf{u}$ is the vorticity, and dissipation rate, $\epsilon = 2\nu S_{ij} S_{ij}$, where S_{ij} is the strain rate, exhibit large local deviations from the mean with their PDF being strongly non-Gaussian⁸⁷. Such small-scale intermittency is one of the central characteristics of the nonlinear dynamics of a fully developed turbulence^{88–90}. Thus, the accuracy with which it can be captured is a sensitive test of the overall quality of the solution. In particular, a question could be asked whether an SES calculation with a much smaller range of available scales compared to the DNS, and thus also

a much smaller spatial ensemble size, can represent accurately the statistics of the velocity-gradient-based quantities.

For the e-HIT cases, Fig. 14 shows the time-averaged PDF of the enstrophy and the dissipation rate normalized by their corresponding mean values. Panels (a) and (b) show that SES- ϵ significantly under-predicts the intermittency of both quantities due to the lower U_{rms} and λ , and thus Re_λ . At the same time, in the SES, statistics of Ω and ϵ are much closer to those in the DNS. In particular, while for enstrophy, the SES PDF is somewhat lower than in the DNS, for dissipation both PDF are in close agreement. Observed discrepancy in the PDF of Ω between the DNS and SES is the result of the relatively low Re_λ of the flow and thus a limited range of scales in the SES. Sufficient separation between the large scales, which are being forced, and the small scales, on which the statistics is collected, is required to minimize the impact of forcing on the latter. Analysis of the intermittency properties in the SES for a wide range of Re_λ will be presented in the follow-up paper.

For the e-HIT SES-SMR tests shown in Fig. 14c,d, PDF generally have worse agreement with the DNS exhibiting suppressed PDF tails at extreme values, which is consistent with the lower Re_λ in these calculations. This disagreement is particularly pronounced in the PDF of dissipation. The only notable exception is the PDF of enstrophy in the SES-SMR3, which is comparable to the SES. Overall, SES-SMR are some-

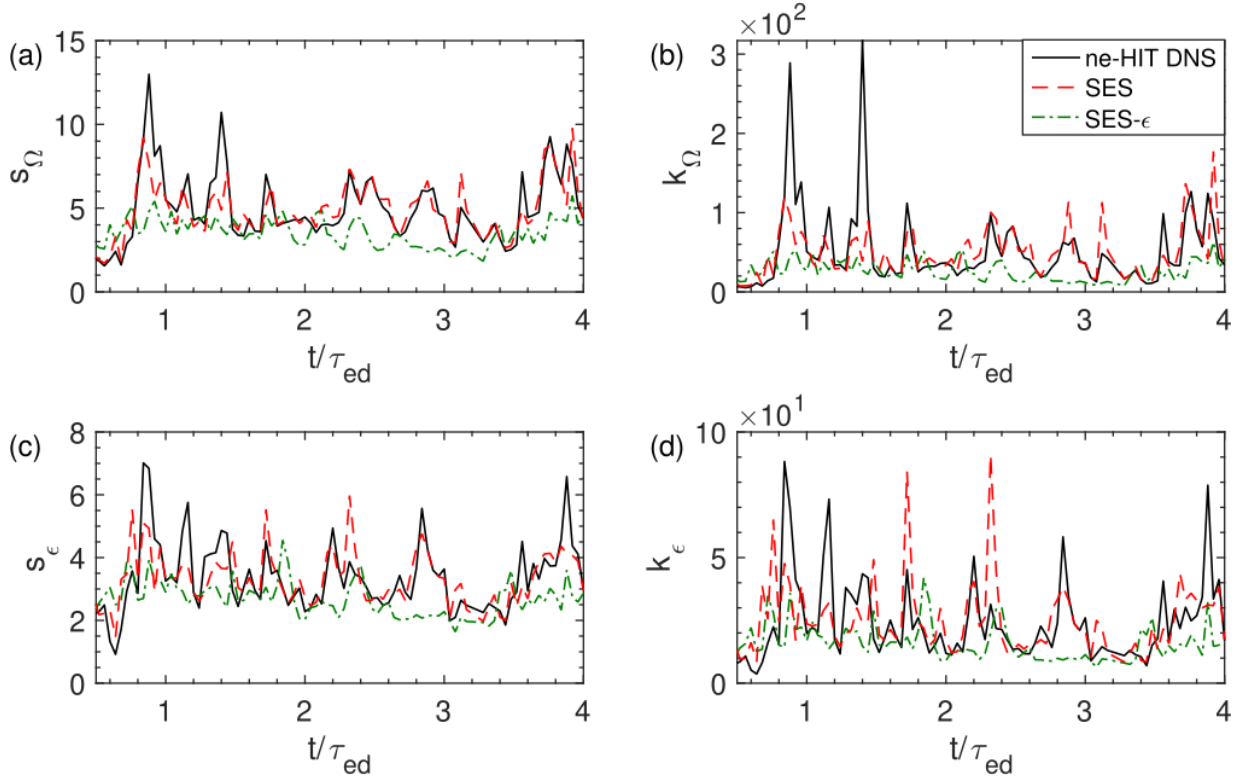


FIG. 15. Skewness (a, c) and kurtosis (b, d) of the PDF of enstrophy, Ω (a, b), and dissipation rate, ε (c, d), in the ne-HIT cases as a function of time. DNS values are shown only for the central region of the domain.

	σ_Ω	s_Ω	k_Ω	b_Ω	σ_ε	s_ε	k_ε	b_ε
DNS	1.89	8.13	182.20	7.04	1.26	4.86	59.75	9.55
SES	1.59	4.68	43.47	8.48	1.14	4.02	37.75	9.98
SES- ε	1.20	3.29	22.36	13.15	0.91	2.28	11.36	16.98
SES-SMR1	1.57	4.34	35.14	8.73	1.09	3.13	19.71	13.28
SES-SMR2	1.58	4.26	33.15	10.84	1.02	2.87	17.12	13.77
SES-SMR3	1.61	4.81	48.30	8.02	1.08	3.15	19.61	11.87

TABLE IV. Statistical parameters of the PDF of enstrophy and dissipation in the e-HIT calculations. See eqs. (39)-(42) for the definitions.

what better able to capture turbulence intermittency than SES- ε , albeit not to the degree of SES.

To compare the obtained statistics more quantitatively, we examine the 2nd-, 3rd-, and 4th-order central moments of both enstrophy and dissipation, i.e., standard deviation, skewness, and kurtosis, defined respectively as

$$\sigma_X = \langle (X - \mu_X)^2 \rangle^{1/2}, \quad (39)$$

$$s_X = \langle (X - \mu_X)^3 \rangle / \sigma_X^3, \quad (40)$$

$$k_X = \langle (X - \mu_X)^4 \rangle / \sigma_X^4, \quad (41)$$

where μ_X is the mean of a given quantity X . Values of these three moments for both quantities are given in Table IV. Obtained DNS values are in agreement with prior findings^{78,87}, and furthermore they are in much closer agreement with the SES than SES-SMR and especially SES- ε .

Another common way to characterize the PDF is by fitting them with the stretched exponential functions⁸⁷

$$f(\psi) \sim \exp(-b_\psi \psi^{1/4}), \quad (42)$$

where ψ is a normalized quantity Ω/μ_Ω or $\varepsilon/\mu_\varepsilon$, and b_ψ is the parameter that gives the best fit of the observed PDF. Stretched exponential fits are typically obtained for values $\psi > 5$, and they are also shown in Fig. 14 as dashed lines. Corresponding values of the parameter b are listed in Table IV. Again, similar to the moments, values of b for the DNS are in agreement with Donzis, Yeung, and Sreenivasan⁸⁷, and they are closer to the SES than to the SES-SMR and SES- ε . In particular, in contrast to the SES, the shapes of the PDF in SES- ε and SES-SMR do not agree well with the stretched exponential functions, especially at the extreme tails.

PDF for the ne-HIT cases cannot be averaged over time.

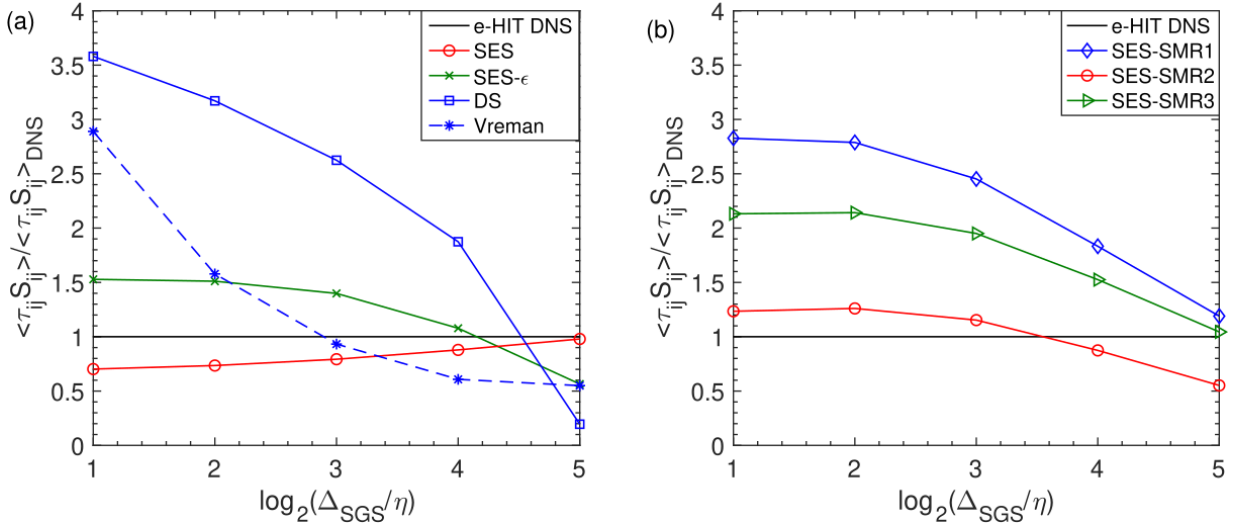


FIG. 16. Time- and space-averaged mean sub-filter scale dissipation, $\langle \tau_{ij} S_{ij} \rangle$, normalized with the DNS results as a function of the filter scale in the e-HIT SES and SES- ϵ (panel a) and in the SES-SMR (panel b). In panel (a), results of the DS and Vreman SGS models are shown for comparison.

Instead, Fig. 15 shows the evolution of skewness and kurtosis of the PDF of enstrophy and dissipation in time both in the DNS and in the SES and SES- ϵ . Note that when considering the instantaneous statistics, only the central DNS region must be compared with the SES due to the large difference in the ensemble size between the central region and the full DNS domain. Once again, SES demonstrates closer agreement with DNS than SES- ϵ . Skewness appears to be better correlated with DNS in time for the SES, compared to kurtosis. In contrast, SES- ϵ shows lower skewness and kurtosis due to the lower Re_λ .

D. LES closures and SGS quantities

The last set of test metrics we describe concerns the accuracy of the proposed L/SES methods in capturing the LES closure terms. A detailed description of the LES equations and the associated unclosed terms is provided in Appendix A. Both in the reference DNS and in the SES calculations, all scales are fully resolved, and thus any unclosed terms of interest can be directly computed by filtering the flow fields.

In weakly compressible low-Mach-number flows, the dominant closure term is the Reynolds stress, τ_{ij} (eq. A4). In particular, since the role of the SGS terms is to describe the effect of small scales, which are primarily dissipative in nature, it is important for the SGS model to produce the correct SGS dissipation, which is given by the product of the Reynolds stress with the resolved strain rate tensor.

As LES closures may be needed at any scale depending on the LES resolution, we compare the sub-filter scale dissipation at several different scales, Δ_{SGS} , by calculating it using the 8th-order differential filter. For the e-HIT cases, it is temporally and spatially averaged and normalized by the corresponding DNS mean. Resulting values are shown in Fig. 16a for the

SES and SES- ϵ , and in Fig. 16b for the SES-SMR tests. To ensure that the same ensemble size is used in the comparison with the DNS values, the spatial average for the reference DNS is taken just over the central sub-region corresponding to the SES.

Obtained results are also compared in Fig. 16a with the two widely used SGS models: the Dynamic Smagorinsky (DS)⁹¹ and Vreman models⁹². For these models, we form a pseudo-LES field by explicitly filtering the resolved DNS data, and then we apply test filters directly on the resulting data. Further summary of the DS and Vreman model coefficients is provided in eqs. (A8)-(A11) and eqs. (A12)-(A15), respectively, in Appendix A. We emphasize that our goal is not to analyze the fidelity of these two models, but rather we provide them here for reference.

Figure 16a shows two opposite trends for the SES and SES- ϵ . At the smallest filter scale close to the Kolmogorov scale, both SES and SES- ϵ are off the target DNS value, with SES being in better agreement with the DNS. However, at larger filter scales, SES values approach the DNS becoming virtually identical with the DNS at $\Delta_{SGS} = 32\eta$ or one half of the SES domain width, which is the filter scale of the SES calculation. This improvement in the accuracy of the sub-filter scale dissipation in the SES on larger scales right up to the scales approaching the inertial range is an important property, as closures are sought at the relevant LES filter scales, which are $\gg \eta$ in practical situations. In contrast, SES- ϵ values start to decrease with increasing Δ_{SGS} becoming approximately half of the DNS value at the largest filter scales. This suggests that SES- ϵ would not be able to provide reliable values of the SGS dissipation on large scales.

All SES-SMR cases show a trend similar to SES- ϵ , though they tend to be much more dissipative. SES-SMR2 produces the closest agreement with DNS at the smaller scales, however its accuracy drops on larger scales reaching $\approx 50\%$ of

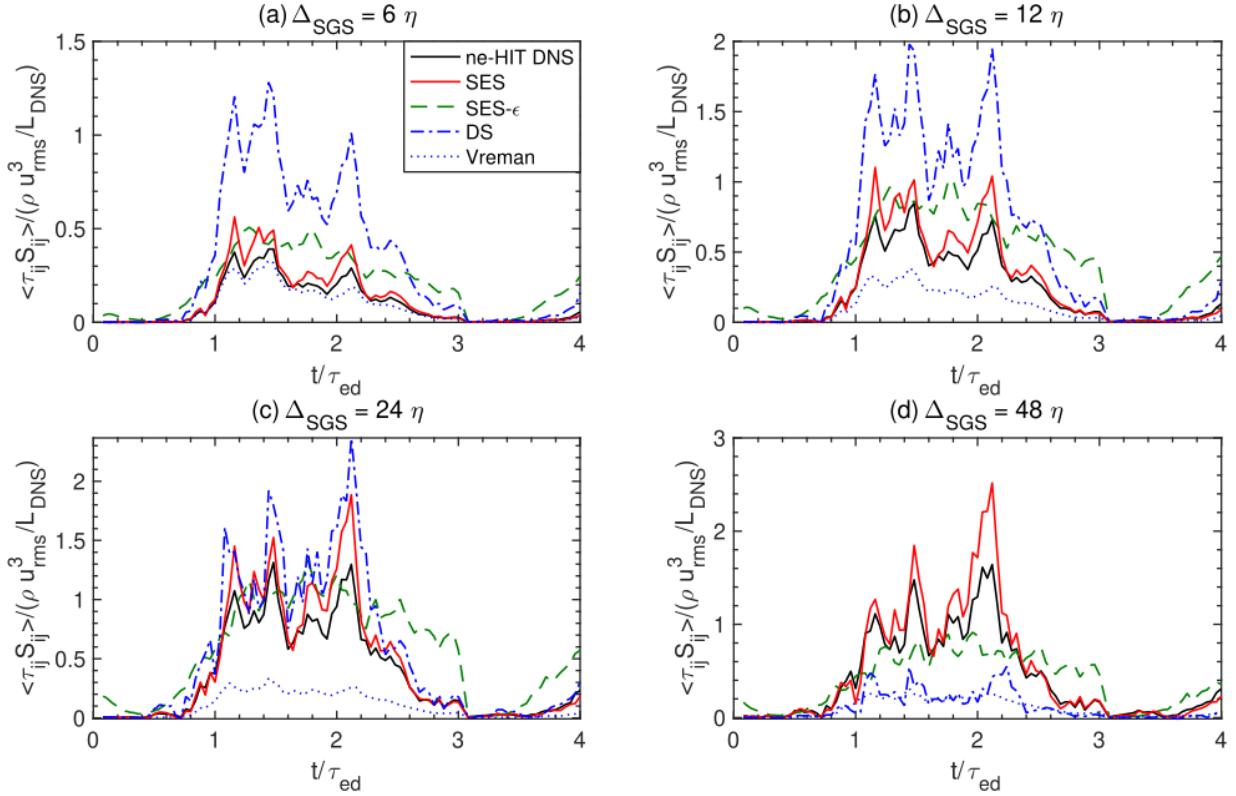


FIG. 17. Mean sub-filter scale dissipation normalized by $U_{rms,DNS}^3/L_{DNS}$ as a function of normalized time at various scales for the ne-HIT case. Spatial averaging is performed only over the central region in the DNS.

the DNS value at the SES filter scale $L_{SES}/2$. In contrast, SES-SMR1 and SES-SMR3 have the worst disagreement with DNS on small scales, but they give better agreement at the largest scales. If LES closures are to be obtained using SMR at some particular scale, it is not clear based on these tests which method of forcing the SMR would be the most appropriate. In general, SMR results tend to disagree with the DNS at most of the scales. This indicates that simply refining the mesh would not allow one to obtain reliable SGS closures.

It is interesting to note that the DS and Vreman models exhibit much worse agreement with DNS than any of the SES tests. In particular, the disagreement is the largest at the smallest dissipative scales close to η . Higher dissipation of these SGS models is in accordance with previous findings^{93,94}. At larger scales, predicted dissipation tends to decrease eventually crossing the DNS values, and at the largest scales, DS and Vreman models tend to under-predict the SGS dissipation.

Finally, for the unsteady ne-HIT, evolution of the spatially averaged sub-filter scale dissipation, which is non-dimensionalized by $\rho U_{rms,DNS}^3/L_{DNS}$, is shown in Fig. 17 for several filter scales. Again, SES shows very close correlation with the DNS values throughout all stages of turbulent growth and decay. This demonstrates the general and flow-agnostic nature of the L/SES, which does not require any calibration for different types of flows. In contrast, SES- ϵ , while exhibiting comparable values to DNS, is virtually uncorrelated with the DNS. Furthermore, both SES and SES- ϵ outperform the existing DS and Vreman models in this unsteady, non-equilibrium

turbulent flow.

VI. DISCUSSION AND CONCLUSIONS

We presented a description of a novel multi-fidelity Large/Small Eddy Simulation (L/SES) method for studying turbulent flows at high Reynolds numbers. The key aspect of the proposed approach is the coupling of a lower-fidelity, unresolved, time-dependent calculation, in particular Large-Eddy Simulation (LES), and a high-fidelity, fully resolved Small-Eddy Simulation (SES) of a small sub-region of interest of the LES. In the present formulation, such coupling between the LES and the SES is one-way and it is provided by continuous replacement of the large scales of the SES flow field with the low-pass filtered velocity field from the LES. Resulting L/SES approach is a combination of both volumetric and boundary forcing. We described all the algorithmic steps of the L/SES approach, including explicit filtering of the LES and SES fields, spatial and temporal interpolation of the large-scale LES data, and the boundary condition treatment.

The L/SES can be viewed as a generalized method for forcing turbulence in resolved simulations, which are effectively embedded in a large-scale flow of arbitrary complexity. In this sense, SES is also a dual counterpart of the traditional LES. In the latter, large-scale structures are explicitly evolved, while the sub-filter scale dynamics is modeled with the appropriate

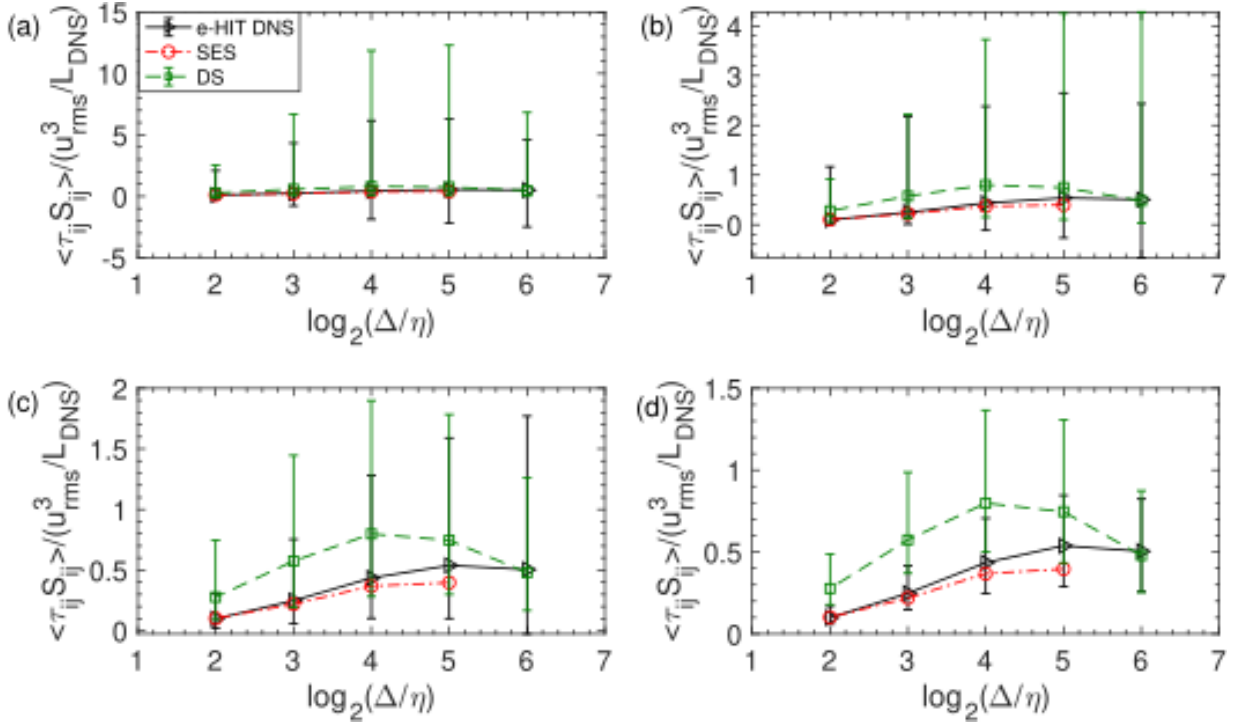


FIG. 18. Time-averaged, normalized SGS dissipation from the entire e-HIT DNS domain at different scales, along with the corresponding DS and SES values. Error bars show the minimum and maximum values of $\langle \tau_{ij} S_{ij} \rangle$ in the sub-regions of different sizes, namely (a) 32^3 cells, (b) 64^3 cells, (c) 128^3 cells, and (d) 256^3 cells. See text for further details.

closures. In contrast, in the SES, small-scale dynamics is explicitly resolved, while the dynamics of the large scales (above the filter scale) not captured in the SES is introduced using the realistic ‘large-scale model’ provided by the companion LES calculation. As such, L/SES is qualitatively different from the traditional turbulence forcing methods, e.g., spectral or linear forcing, which are idealized in nature and are thus decoupled from any large-scale flow properties.

Proposed approach is applicable for an arbitrary geometry, as well as any initial and boundary conditions, as long as the filtering operation can be applied in the physical space. L/SES does not make assumptions of periodicity or turbulence equilibrium, and it is agnostic to any underlying flow features such as anisotropy or shear, which can be captured directly without additional modifications. Thus, L/SES is potentially applicable to complex turbulent flows in practical physical and engineering systems. We demonstrated the method performance in the *a priori* tests of both steady and unsteady (including decaying) homogeneous, isotropic turbulence (HIT). Analysis of the method accuracy in more complex turbulent flows will be presented in future work.

The only implicit assumption made in the L/SES is that the large scales in the LES are sufficiently accurate. Furthermore, one-way coupling between the LES and the SES in the current formulation also implies that the large-scale dynamics is not critically controlled by the small scales. This is reasonable for the flows, which are dominated by the downward cascade of kinetic energy on average, such as HIT considered in the *a priori* tests described here. Although such flows would

also contain regions where the upscale transfer, or backscatter, of kinetic energy is locally observed^{95,96}, the net effect of such backscatter on the large scales is limited. Furthermore, since the SES domain is not periodic, any transfer of kinetic energy to scales larger than L_{SES} will be able to leave the domain, thus maintaining the accuracy of the small scales. At the same time, special treatment would be required in the flows with a strong kinetic energy backscatter or net up-scale transfer of kinetic energy. This is the case, for instance, in reacting flows^{56–58}, in which small scales can efficiently energize the large scales in the turbulent flame, and thus large-scale dynamics may not necessarily be determined independently of the small scales. In such cases, a two-way coupling between the SES and the parent LES is necessary, which is a subject of future work.

In the context of such two-way coupling, an important question is whether L/SES can be used to provide the closures for the LES calculation directly without the need for their modelling. Presented *a priori* tests demonstrate that SES can indeed give the correct SGS dissipation in the sub-region of interest, outperforming the classically used closure models, such as the Dynamic Smagorinsky (DS) and Vreman models^{91,92}. In particular, in addition to the close agreement of the mean $\langle \tau_{ij} S_{ij} \rangle$ in the equilibrium HIT, L/SES also achieves good temporal correlation with the DNS in the time-evolving, non-equilibrium HIT.

The key aspect here, however, is that the SES domain is restricted to a pre-selected sub-region of the larger flow, and as a result, it can provide the SGS closures only in that par-

ticular region. At the same time, even in the ideal case of a steady-state HIT, the instantaneous values of the relevant quantities, such as the SGS dissipation, could differ significantly between various sub-regions⁹⁷. Such variability is illustrated in Fig. 18. In particular, black symbols show the normalized SGS dissipation at different scales in the e-HIT DNS. These values are calculated by explicitly filtering the fully-resolved DNS data, and subsequently averaging resulting values temporally and spatially over the entire 1024^3 domain. Green symbols also show the average values of the SGS dissipation obtained using the DS model at the same scales. Next, we partition the entire DNS domain into smaller sub-regions with sizes ranging from 32^3 cells to 256^3 cells. For each particular sub-region size, the average SGS dissipation, $\langle \tau_{ij} S_{ij} \rangle$, is calculated in each sub-region both directly from the DNS data and using the DS model. Resulting minimum and maximum values among all sub-regions are shown with error bars in Fig. 18. For comparison, $\langle \tau_{ij} S_{ij} \rangle$ in the SES domain, which corresponds to the central 128^3 sub-region of the DNS, is also shown with red symbols. As can be seen, there is significant variability in the mean SGS dissipation between different sub-regions of the flow at all scales and for all sub-region sizes. This variability can result in an order of magnitude deviation of $\langle \tau_{ij} S_{ij} \rangle$ from the global mean, particularly for smaller region sizes. An SGS model, such as DS, which is computed everywhere in the flow, also exhibits variability in different sub-regions, although agreement with the DNS, both in terms of the mean values, as well as the observed minimum/maximum range, can be quite poor.

In contrast, the SES captures the mean SGS dissipation in the DNS quite well. At the same time, since SES is only performed for the central region, by definition it cannot describe the variability of the dissipation throughout the entire flow. Therefore, a single SES calculation cannot provide SGS closures for a more extended region of the host large-scale flow, or for the entire LES calculation. This is not necessarily a shortcoming of the method, as it is inherent in the formulation itself, whereby the SES can only accurately capture the flow structure in the region, which was used to force it.

At the same time, L/SES fundamentally differs from the traditional LES in that it provides closure terms directly from first principles, without any assumptions or approximations. Such ability to correctly recover sub-filter quantities can be useful to validate new LES models or verify their applicability in the poorly explored regimes. L/SES can also serve as a useful discovery tool to probe specific LES regions with higher fidelity. If the large-scale flow is non-homogeneous, multiple SES may be required to probe different sub-regions with sufficiently distinct small-scale dynamics. Therefore, L/SES can serve as a tool for the development of the SGS models, which can then be used to provide two-way coupling with the LES.

It is important also to highlight the differences between the proposed L/SES approach and the existing data assimilation techniques including various nudging methods. For instance, Clark Di Leoni, Mazzino, and Biferale⁴⁴ applied nudging in homogeneous and isotropic turbulence, with the reference data obtained from a DNS and injected either at isolated locations in physical space or at a set of spectral modes. In

particular, the latter spectral case is analogous to the L/SES approach in that the reference data was Fourier filtered at low wavenumbers. At the same time, such methods differ from the L/SES in two key respects. First, from the fundamental standpoint, traditional data assimilation assumes that the reference data is a true solution obtained either through the experiments/observations or in a high-fidelity simulation⁴⁴. As a result, the principal goal of such techniques is to reach synchronization between the reference field and the obtained solution. Achieving such synchronization for the entire spectral range is a non-trivial task, especially when only a subset of the wavenumbers are nudged. Indeed, as shown by Clark Di Leoni, Mazzino, and Biferale⁴⁴, the error between the reference field and the obtained solution is low only for the wavenumbers being nudged, in particular at large scales. This in turn raises the question of the accuracy of the solution on scales, on which such synchronization is not reached. In contrast, in the L/SES, the forcing field is obtained from a low-fidelity solution, in which by definition small-scale structure cannot be assumed to be accurate and is therefore discarded. L/SES does not require the availability of the true reference solution, which in many cases may be difficult or impossible to obtain, and thus, by construction, there is no goal to achieve the synchronization for the entire range of scales. Crucially, we show that even using a low-fidelity reference solution, the cost of obtaining which may be relatively low, it is possible to recover the small-scale flow structure very accurately. Second, from a practical standpoint, traditional spectral nudging techniques^{41,44} rely on spectral decomposition of the reference field and thus they cannot be directly applied in physical space. This limits their utility in the engineering contexts, which may not have periodic boundary conditions and simple geometries. Proposed L/SES approach does not have this limitation as it is entirely formulated in physical space, which requires various algorithmic steps described in § II above. Moreover, for periodic cases such as HIT, the relaxation of the periodicity requirement allows L/SES to be used in sub-regions of the large-scale flows, thereby potentially allowing reduction in computational cost and access to large Reynolds numbers even in such idealized geometries.

We also described two alternative approaches for embedding a high-resolution calculation in a sub-region of interest of a larger turbulent flow. In particular, the L/SES- ε method extracts the rate of the inter-scale energy transfer in that sub-region and uses it as a time-dependent energy injection rate in the SES calculation. This approach is effectively a generalization of the traditional class of the volumetric spectral forcing techniques, albeit in which the energy injection rate is not specified as an ad hoc parameter, but instead directly determined from the LES. The L/SES- ε method, however, still reduces the entire large-scale flow structure to a single scalar parameter based only on the inter-scale kinetic energy transfer rate. Various obtained small-scale statistics suggest that an independent simulation, forced using such energy injection rate, results in a much lower Re_λ , thereby leading to much lower values of U_{rms} as well as inaccurate statistics of the small-scale flow quantities, such as enstrophy or dissipation.

In this regard, a more specific observation can be made

based on the *a priori* tests described above. In particular, one can consider an idealized case of the HIT turbulence and compare a DNS of a larger flow with an SES- ε corresponding to a smaller sub-region of such a DNS, with both calculations forced with the same volumetric energy injection rate, thereby leading to the same average dissipation rate. The flow solution in the SES- ε will not represent the corresponding sub-region of the larger flow even in the statistically averaged sense. In particular, while SES- ε can recover the same mean dissipation rate and kinetic energy spectrum representative of the large-scale flow in line with the Kolmogorov '41 theory, it fails to capture the correct total kinetic energy content in the region of interest or the small-scale statistics of the velocity gradients. This suggests that classical volumetrically forced DNS driven in a conventional way through energy injection at the largest scale with a constant rate cannot be considered to represent a small section of a larger external flow at the same Reynolds number.

In addition to the traditional volumetric forcing, we also contrasted the L/SES with a boundary forcing approach, in which a high-resolution region is directly embedded in a larger flow using static (or adaptive) mesh refinement. In this case, such refined region embedded in an LES interacts with the coarser regions directly through the coarse-fine interfaces. This direct embedding somewhat increases the resulting flow Reynolds number in the high-resolution region compared to the volumetric-only L/SES- ε approach, however agreement in Re_λ and other small-scale flow statistics with the DNS is still worse than for the L/SES.

Comparison of the accuracy of the L/SES approach with the L/SES- ε and L/SES-SMR raises a more fundamental question regarding the nature of the interaction between various scales of turbulence. The inability of L/SES- ε to match the Re_λ of the large-scale flow shows that a single scalar, even representing accurately the inter-scale energy transfer rate, does not capture all the relevant information transmitted from the large to small scales. In particular, since this scalar is obtained at a specific filter scale $\Delta = L_{SES}$, which is equal to the SES- ε forcing scale, this indicates that using information only from scales close to the driving scale is insufficient to replicate the small-scale behavior of the underlying flow. To investigate this further, an L/SES simulation was performed, which used the band-pass-filtered forcing data extracted from scales in the range from L_{SES} to $2L_{SES}$. This produced much worse results than the regular L/SES approach, which uses low-pass filtered forcing data, and thus incorporates all scales $> \Delta$. Results of this test are not shown here for brevity. This suggests that in a turbulent flow, the transfer of information does not occur only between the adjacent wavenumbers, but rather through a complex interaction of all scales^{98–100}. This is further corroborated by a somewhat better accuracy of the L/SES-SMR approach, in which the refined region is allowed to interact with all larger scales of the ambient flow through the boundaries. At the same time, the fact that even L/SES-SMR was not able to achieve the same solution fidelity as the L/SES shows that capturing the small-scale complexity of a larger host flow cannot be achieved by merely driving a single wavenumber or forcing through just the domain boundaries. Forcing of the

embedded calculation must be volumetric in nature affecting the entire domain, in both physical and spectral space.

An additional comment should be made regarding the overall formulation of the L/SES approach. Governing equations for the small-scale flow field can be directly derived by subtracting the filtered LES equations from the Navier-Stokes equations. Such equations would directly describe the evolution of the fluctuating quantities on scales smaller than the desired filter scale. Depending on the definition of the fluctuating quantities, two forms of such equations can be obtained, which are given in Appendix B (also see Rah, Dhandapani, and Blanquart³⁴). Instead of the forcing described in § II, either set of equations could be used to evolve the SES solution. Resulting formulation is directly dual to the LES equations as the small-scale quantities are evolved and the large-scale flow is represented with the filtered quantities appearing as closure terms on the right-hand side of the equations. Such closure terms can be obtained directly from the LES data, thus eliminating the need for the closed-form closure models for the large-scale flow.

At the same time, equations given in Appendix B present several drawbacks compared to the proposed L/SES procedure. The first set of equations (B1)-(B3) for the fluctuating primitive variables involves source terms in the mass conservation equation (B1), which is undesirable. This, however, can be remedied using the second set of equations (B9)-(B11) at the expense of more complex definitions of the fluctuating quantities (eqs. B7 and B8). Furthermore, both sets of equations include terms, which involve products of filtered and fluctuating quantities. For instance, the transport equation (B10) of the fluctuating momentum M'_i depends not only on the advection of M'_i by the fluctuating velocity u''_j , but also on the advection of the filtered momentum \bar{M}_i by u''_j and of M'_i by the filtered velocity \bar{u}_j . Furthermore, unclosed LES terms such as R_{ij} are also present and must be obtained by first calculating the total velocity, taking the product of its components, and explicitly filtering the result. Therefore, the filtered and fluctuating fields cannot be completely isolated from each other and the above procedure does not have any advantage over the proposed L/SES method. Finally and most importantly, since LES filtered quantities appear in the source terms, they would affect all SES scales directly. This is in contrast with the proposed L/SES, in which the LES data is used only to drive the large SES scales, while the small scales are allowed to develop naturally. Due to these considerations, the transport equations for the fluctuating small-scale quantities were not considered further in this work.

Present work provides a demonstration of the L/SES method for a canonical flow, namely HIT. At the same time, several open issues merit further investigation. First, the key step of the approach, which separates information at various scales, is the filtering operation applied in the physical space. Since the method is intended for the arbitrary boundary conditions, perfect spectrally sharp filtering is not possible. Therefore, an important future step for the improvement of the overall method involves the development of the filters with more desirable properties, as discussed in § II A 1. Such improved filters would not only increase the accuracy of the method,

but they would also reduce the computational cost by reducing spectral leakage and thus maximizing the range of scales available for analysis. Furthermore, it is desirable to design filters, which can work with the smaller sponge and buffer regions. Reducing the extent of such regions is important when the chosen SES domain lies close to a physical boundary of the LES, e.g., near a wall, where additional sponge and buffer region data may not be available.

We also note that since present work considered only the *a priori* tests, various aspects of the method related to the LES calculations were not explored. More specifically, this concerns the choice of the filter scale relative to the LES grid size, Δ/dx_{LES} , as well as the overall accuracy of the LES solution and the potential effect of the SGS closure models. There would always exist a discrepancy between the flow field obtained in an LES and the true Navier-Stokes solution. Such discrepancy, however, would be the largest at the small LES scales, which are most affected by the lack of resolution. Therefore, for *a posteriori* SES, the filter scale Δ would need to be sufficiently larger than the smallest scales that the LES resolves, and of the order of the Taylor scale λ . Explicit filtering of the LES data at scale Δ would then ensure that such unphysical small scales are removed thereby minimizing their impact on the SES forcing. These aspects will be presented in detail in the follow-up paper focusing on the *a posteriori* tests for a range of Re_λ . Finally, it would be interesting in the future to analyze the sensitivity of the SES solution to the potential errors in the large-scale component of the LES flow field in the *a priori* sense by introducing noise or systematic bias in the large-scale DNS velocities.

Another important extension of the L/SES approach concerns compressible turbulent regimes. In this work, the focus was on the weakly compressible HIT. As a result, forcing the velocity field (eq. 1) or the momentum (eq. 3) yielded virtually identical results. This would not be the case for more complex flows. For instance, in compressible HIT, perturbing the momentum instead of velocity would be more appropriate. For other situations, such as boundary or shear layers, scalar mixing, or reacting flows, forcing of other quantities such as energy (or pressure) and scalars may be necessary to recover proper structure not only of the velocity field, but also of the fields of passive and active scalars. Such extension of the L/SES approach to compressible, as well as variable density flows is an important future step.

Notwithstanding these current limitations of the L/SES, proposed approach presents a number of important advantages. Since the large scales are directly imposed in the SES, all their complexity is injected into the small-scale calculation. This makes the L/SES a versatile forcing technique, which incorporates all the relevant large-scale features by design, eliminating the need for the flow-dependent modifications. It is also a fundamentally different approach from LES modelling, as it allows one to obtain closure terms in the region of interest directly from first principles, without any assumptions or approximations.

Finally, one of the key advantages of the L/SES method is its ability to recover the detailed small-scale flow structure, including the highly intermittent statistics of the velocity-

gradient-based quantities corresponding to the Reynolds number of the actual flow of interest. This opens the possibility for probing the high-Reynolds-number flow regimes, which are largely inaccessible in the DNS, with fully resolved simulations. Such calculations can be performed at a fraction of the computational cost of a full DNS due to the combination of a coarse LES and a well-resolved SES in a smaller sub-region. Detailed exploration of this aspect of the L/SES method, and the demonstration of the computational advantage of the L/SES in comparison with the DNS, will be presented in the follow-up paper, which will focus on the *a posteriori* tests for a wide range of Reynolds numbers.

ACKNOWLEDGMENTS

Authors acknowledge funding support from NASA under award 80NSSC22K0630 (technical officer: Dr. Sanaz Vahidinia), Air Force Office of Scientific Research (AFOSR) under award FA9550-21-1-0012 (program manager: Dr. Chipping Li), as well as the University of Connecticut Research Excellence Program. Computing resources were provided by the Department of Defense High Performance Computing Modernization Program (HPCMP). Authors are also grateful to Diego Donzis and George Matheou for valuable discussions.

DATA AVAILABILITY

Raw data were generated at the Department of Defense HPCMP facilities. Derived data supporting the findings of this study are available from the corresponding author upon reasonable request.

AUTHOR DECLARATIONS

Author contributions

Arnab Moitro: Conceptualization (equal); Data curation (lead); Formal analysis (lead); Investigation (lead); Methodology (equal); Software (lead); Validation (lead); Visualization (lead); Writing – original draft (lead); Writing – review & editing (equal). **Sai Sandeep Dammati:** Data curation (supporting); Formal analysis (supporting); Software (supporting); Visualization (supporting); Writing – review & editing (supporting). **Alexei Poludnenko:** Conceptualization (equal); Data curation (supporting); Funding acquisition; Supervision; Methodology (equal); Writing – original draft (supporting); Writing – review & editing (equal).

Conflict of interest

The authors have no conflicts to disclose.

Appendix A: LES subgrid-scale closures and Reynolds stress estimates

Here, for completeness, we include the LES equations along with the associated unclosed subgrid-scale (SGS) terms, in particular the Reynolds stress term, which is compared between the DNS and SES in § V D. We also describe two reference closure models, namely Dynamic Smagorinsky⁹¹ and Vreman⁹² models, which are used in the comparisons in § V D.

LES do not resolve the small scales of turbulent motion. Instead, they solve the low-pass filtered Navier-Stokes equations¹⁰¹

$$\frac{\partial \bar{p}}{\partial t} + \frac{\partial \bar{p} \tilde{u}_j}{\partial x_j} = 0, \quad (\text{A1})$$

$$\frac{\partial \bar{p} \tilde{u}_i}{\partial t} + \frac{\partial \bar{p} \tilde{u}_i \tilde{u}_j}{\partial x_j} + \frac{\partial \bar{p}}{\partial x_i} - \frac{\partial \tilde{\sigma}_{ij}}{\partial x_j} = -\frac{\partial \tau_{ij}}{\partial x_j}, \quad (\text{A2})$$

$$\begin{aligned} \frac{\partial \bar{p} \tilde{E}}{\partial t} + \frac{\partial (\bar{p} \tilde{E} + \bar{p}) \tilde{u}_j}{\partial x_j} - \frac{\partial \tilde{\sigma}_{ij} \tilde{u}_i}{\partial x_j} + \frac{\partial \tilde{q}_j}{\partial x_j} \\ - \frac{\partial}{\partial x_j} (\gamma c_V Q_j + \frac{J_j}{2} - D_j). \end{aligned} \quad (\text{A3})$$

Here, calorically perfect gas is assumed, $\bar{\phi}$ and $\tilde{\phi} = \overline{\rho \phi} / \bar{\rho}$ represent Reynolds and Favre filtering of a quantity ϕ , respectively. The $\tilde{q}_j = -\tilde{k} \partial \tilde{T} / \partial x_j$ and $E = e + u_k u_k / 2$, where e is the internal energy per unit mass and c_V is the heat capacity at constant volume.

Filtering gives rise to the unclosed SGS terms on the right-hand sides of eqs. (A2)-(A3), which cannot be obtained directly from the filtered flow variables and instead need to be modelled. They have the following form

$$\tau_{ij} = \bar{\rho} (\widetilde{u_i u_j} - \tilde{u}_i \tilde{u}_j), \quad (\text{A4})$$

$$Q_j = \bar{\rho} (\widetilde{u_j T} - \tilde{u}_j \tilde{T}), \quad (\text{A5})$$

$$J_j = \bar{\rho} (\widetilde{u_j u_k u_k} - \tilde{u}_j \widetilde{u_k u_k}), \quad (\text{A6})$$

$$D_j = \bar{\sigma}_{ij} \tilde{u}_i - \tilde{\sigma}_{ij} \tilde{u}_i. \quad (\text{A7})$$

Here τ_{ij} is the Reynolds stress, Q_j is the SGS heat flux, while J_j and D_j describe the SGS turbulent diffusion and viscous dissipation. The equation of state, $p = \rho RT$, has been used to represent the pressure gradient in terms of the SGS heat flux. Laminar diffusive fluxes, $k \frac{\partial T}{\partial x_j} - \tilde{k} \frac{\partial \tilde{T}}{\partial x_j}$, are small compared to the turbulent transport and they typically can be ignored¹⁰².

The Reynolds stress τ_{ij} is the most important closure term to consider in the simulations of low-Mach-number, weakly compressible turbulence, which is the case in this study. SGS closure terms in the energy conservation equation (A3) in such low-Mach regimes are orders of magnitude smaller than their filtered counterparts at all scales and thus can be ignored^{103,104}. Assessment of their accuracy in the SES, along with the analysis of the L/SES method performance in compressible regimes, is the subject for future work.

For comparison with the direct calculation of τ_{ij} in the SES discussed in § V D, we consider two widely used SGS models, namely Dynamic Smagorinsky (DS)⁹¹ and Vreman models⁹². The ‘true’ model coefficients are calculated using a pseudo-LES field formed by filtering the DNS, and then applying test filters directly on the resultant data.

The DS model closures are calculated as

$$\tau_{kl} - \frac{1}{3} q^2 \delta_{kl} = 2C \bar{\rho} \Delta^2 |\tilde{S}| (\tilde{S}_{kl} - \frac{1}{3} \tilde{S}_{mm} \delta_{kl}), \quad (\text{A8})$$

$$\begin{aligned} \tilde{S}_{kl} = \frac{1}{2} \left(\frac{\partial \tilde{u}_k}{\partial x_l} + \frac{\partial \tilde{u}_l}{\partial x_k} \right), \quad |\tilde{S}| = (2 \tilde{S}_{kl} \tilde{S}_{kl})^{1/2}, \\ q^2 = 2C_I \bar{\rho} \Delta^2 |\tilde{S}|^2, \end{aligned} \quad (\text{A9})$$

$$C_I = \frac{\langle L_{kk} \rangle}{\langle 2 \hat{\rho} \hat{\Delta}^2 |\hat{S}|^2 - 2 \Delta^2 \bar{\rho} |\hat{S}|^2 \rangle}, \quad (\text{A10})$$

$$L_{kl} = \widehat{\rho \tilde{u}_k \tilde{u}_l} - (1/\hat{\rho}) (\widehat{\rho \tilde{u}_k} \widehat{\rho \tilde{u}_l}),$$

$$C = \frac{\langle L_{kl} \tilde{S}_{kl} - (1/3) \tilde{S}_{mm} L_{jj} \rangle}{C_D}, \quad (\text{A11})$$

$$\begin{aligned} C_D = \langle -2 \hat{\rho} \hat{\Delta}^2 |\hat{S}| (\hat{S}_{kl} \tilde{S}_{kl} - (1/3) \hat{S}_{mm} \tilde{S}_{jj}) \\ + 2 \Delta^2 (\bar{\rho} |\tilde{S}| \widehat{\tilde{S}_{kl} \tilde{S}_{kl}} - (1/3) \bar{\rho} |\tilde{S}| \widehat{\tilde{S}_{mm} \tilde{S}_{jj}}) \rangle \end{aligned}$$

Here, $\widehat{\dots}$ represents the Favre-filtered DNS variables mimicking the LES data, and $\hat{\dots}$ represents explicit test filtering of the filtered DNS variable. The test filter width $\hat{\Delta}$ is chosen to be twice the width of the scale, at which the closure is desired, i.e., $\hat{\Delta} = 2\Delta$. Model coefficients obtained from the DNS were found to be $C = 0.21$ and $C_I = 0.014$, in agreement with the findings of Fureby *et al.*⁹⁴.

Closures using the Vreman model are calculated as

$$\langle \tau_{ij} \rangle = \langle -2\nu_e \tilde{S}_{ij} + \frac{2}{3} k_\tau \delta_{ij} \rangle, \quad k_\tau = 2\nu_e |\tilde{S}| \quad (\text{A12})$$

$$\nu_e = c \sqrt{\frac{B_\beta}{\alpha_{ij} \alpha_{ij}}}, \quad c = 2.5 C_S^2, \quad (\text{A13})$$

$$\alpha_{ij} = \frac{\partial \tilde{u}_j}{\partial x_i}, \quad \beta_{ij} = \Delta^2 \alpha_{mi} \alpha_{mj}, \quad (\text{A14})$$

$$\begin{aligned} B_\beta = \beta_{11} \beta_{22} - \beta_{12}^2 + \beta_{11} \beta_{33} - \beta_{13}^2 \\ + \beta_{22} \beta_{33} - \beta_{23}^2. \end{aligned} \quad (\text{A15})$$

Here, the suggested value of $C_S = 0.17$ is used⁹², and the rest of the symbols have the same meaning as above.

Appendix B: Governing equations for fluctuating quantities

Here, we describe the evolution equations for the small-scale fluctuating component of the flow field, which provide an alternative formulation to the L/SES proposed above. These equations are obtained by subtracting the filtered LES equations (A1)-(A3) from the Navier-Stokes equations. In particular, consider the fluctuating components of any quantity ϕ , namely $\phi' = \phi - \bar{\phi}$ and $\phi'' = \phi - \tilde{\phi}$, where $\bar{\phi}$ and $\tilde{\phi}$ represent Reynolds and Favre filtering, respectively.

For the fluctuating primitive variables, ρ' , u'' , and e'' , the governing equations take the form

$$\frac{\partial \rho'}{\partial t} + \frac{\partial \rho' u_j'}{\partial x_j} = -\frac{\partial}{\partial x_j} (\bar{\rho} u_j'' + \rho' \tilde{u}_j), \quad (\text{B1})$$

$$\begin{aligned} & \left(\frac{\partial \rho' u_i''}{\partial t} + \frac{\partial \rho' u_i' u_j''}{\partial x_j} \right) + \\ & \left(\frac{\partial \bar{\rho} u_i''}{\partial t} + \frac{\partial}{\partial x_j} (\bar{\rho} u_i'' (u_j'' + \tilde{u}_j)) \right) + \\ & \left(\frac{\partial \rho' \tilde{u}_i}{\partial t} + \frac{\partial}{\partial x_j} (\rho' \tilde{u}_i (u_j'' + \tilde{u}_j)) \right) = \\ & -\frac{\partial \rho'}{\partial x_i} - \frac{\partial R_{ij}}{\partial x_j} - \frac{\partial}{\partial x_j} (\bar{\rho} \tilde{u}_i u_j'' + \rho' u_i'' \tilde{u}_j), \end{aligned} \quad (\text{B2})$$

$$\begin{aligned} & \left(\frac{\partial \rho' e''}{\partial t} + \frac{\partial \rho' e'' u_j''}{\partial x_j} \right) + \\ & \left(\frac{\partial \bar{\rho} e''}{\partial t} + \frac{\partial}{\partial x_j} (\bar{\rho} e'' (u_j'' + \tilde{u}_j)) \right) + \\ & \left(\frac{\partial \rho' \tilde{e}}{\partial t} + \frac{\partial}{\partial x_j} (\rho' \tilde{e} (u_j'' + \tilde{u}_j)) \right) = \\ & -\rho' \frac{\partial u_j''}{\partial x_j} + \frac{\partial q_j'}{\partial x_j} + \frac{\partial Q_j}{\partial x_j} - \alpha_P^{SGS} - \\ & \left(\bar{p} \frac{\partial u_j''}{\partial x_j} + \rho' \frac{\partial \tilde{u}_j}{\partial x_j} \right) - \frac{\partial}{\partial x_j} (\bar{p} \tilde{e} u_j'' + \rho' e'' \tilde{u}_j). \end{aligned} \quad (\text{B3})$$

Here, the equation of state has the usual form $p' = (\gamma - 1) \bar{p} e''$. The closure terms are

$$R_{ij} = -\bar{\rho} (\overline{u_i \tilde{u}_j} - \tilde{u}_i \tilde{u}_j), \quad (\text{B4})$$

$$\alpha_P^{SGS} = -\left(\bar{p} \frac{\partial u_j''}{\partial x_j} - \bar{p} \frac{\partial \tilde{u}_j}{\partial x_j} \right), \quad (\text{B5})$$

$$Q_j = -\bar{\rho} (\overline{e u_j} - \tilde{e} \tilde{u}_j). \quad (\text{B6})$$

In this form, governing equations are quite complex, they do not have the usual conservative flux form, and furthermore even the mass continuity equation (B1) has a source term.

An alternative set of equations can be formulated if we introduce modified fluctuating momentum M_i' and fluctuating internal energy per unit volume, which are defined as

$$M_i' = \bar{\rho} u_i'' + \rho' \tilde{u}_i + \rho' u_i'', \quad (\text{B7})$$

$$E' = \bar{\rho} e'' + \rho' \tilde{e} + \rho' e''. \quad (\text{B8})$$

In this case, governing equations take on the following form

$$\frac{\partial \rho'}{\partial t} + \frac{\partial M_j'}{\partial x_j} = 0, \quad (\text{B9})$$

$$\begin{aligned} \frac{\partial M_i'}{\partial t} + \frac{\partial M_i' u_j''}{\partial x_j} = & -\frac{\partial p'}{\partial x_i} - \frac{\partial R_{ij}}{\partial x_j} \\ & - \frac{\partial}{\partial x_j} (\bar{M}_i u_j'' + M_i' \tilde{u}_j), \end{aligned} \quad (\text{B10})$$

$$\begin{aligned} \frac{\partial E'}{\partial t} + \frac{\partial (E' + p') u_j''}{\partial x_j} = & \frac{\partial q_j'}{\partial x_j} + \frac{\partial Q_j}{\partial x_j} \\ & - \frac{\partial}{\partial x_j} (\bar{E} u_j'' + E' \tilde{u}_j) - \alpha_P^{SGS} - \left(\bar{p} \frac{\partial u_j''}{\partial x_j} + \rho' \frac{\partial \tilde{u}_j}{\partial x_j} \right). \end{aligned} \quad (\text{B11})$$

Here, filtered conserved variables are defined as $\bar{M}_i = \bar{\rho} \tilde{u}_i$ and $\bar{E} = \bar{\rho} \tilde{e}$. The equation of state becomes $p' = (\gamma - 1) E' = (\gamma - 1) (\bar{\rho} e'' + \rho' \tilde{e} + \rho' e'')$. In this formulation, governing equations take on a simpler and more familiar conservative flux form. They also avoid the source terms in the mass continuity equation at the expense of more complex definitions of the fluctuating momentum and energy, which involve both fluctuating and filtered primitive variables. Finally, note that viscous terms are not included in both sets of equations because we only intend to demonstrate the complexity of such an approach rather than formulate the full set of governing equations.

- ¹S. Ghosal, M. Rogers, and A. Wray, "The turbulent life of phytoplankton," Center for Turbulence Research, 31–45 (2000).
- ²S. B. Sadykova, A. M. Dostiyarov, M. G. Zhumagulov, and N. R. Kartjanov, "Influence of turbulence on the efficiency and reliability of combustion chamber of the gas turbine," *Thermal Science* **25**, 4321–4332 (2021).
- ³E. A. D'Asaro, "Turbulence in the upper-ocean mixed layer," *Annual Review of Marine Science* **6**, 101–115 (2014).
- ⁴M.-M. Mac Low and R. S. Klessen, "Control of star formation by supersonic turbulence," *Reviews of Modern Physics* **76**, 125 (2004).
- ⁵A. Y. Poludnenko, J. Chambers, K. Ahmed, V. N. Gamezo, and B. D. Taylor, "A unified mechanism for unconfined deflagration-to-detonation transition in terrestrial chemical systems and type Ia supernovae," *Science* **366**, eaau7365 (2019).
- ⁶J. Jimenez and R. D. Moser, "Large-eddy simulations: where are we and what can we expect?" *AIAA journal* **38**, 605–612 (2000).
- ⁷S. B. Pope, "Turbulent Flows," (2001).
- ⁸P. Sagaut, *Large eddy simulation for incompressible flows: an introduction* (Springer Science & Business Media, 2005).
- ⁹H. Tennekes and J. L. Lumley, *A first course in turbulence* (MIT press, 1972).
- ¹⁰P. R. Spalart, "Detached-eddy simulation," *Annual Review of Fluid Mechanics* **41**, 181–202 (2009).
- ¹¹Y. Zhiyin, "Large-eddy simulation: Past, present and the future," *Chinese Journal of Aeronautics* **28**, 11–24 (2015).
- ¹²D. Corson, R. Jaiman, and F. Shakib, "Industrial application of RANS modelling: Capabilities and needs," *International Journal of Computational Fluid Dynamics* **23**, 337–347 (2009).
- ¹³P. Moin and K. Mahesh, "Direct numerical simulation: a tool in turbulence research," *Annual review of fluid mechanics* **30**, 539–578 (1998).
- ¹⁴M. Quadrio, B. Frohnapfel, and Y. Hasegawa, "Does the choice of the forcing term affect flow statistics in DNS of turbulent channel flow?" *European Journal of Mechanics-B/Fluids* **55**, 286–293 (2016).

- ¹⁵R. Dhariwal and S. L. Rani, "Forcing in DNS of stationary isotropic turbulence and its effects on the closure of diffusion current in the PDF kinetic equation for high-inertia particle pairs," *International Journal of Multiphase Flow* **155**, 104187 (2022).
- ¹⁶R. Das and S. S. Girimaji, "The effect of large-scale forcing on small-scale dynamics of incompressible turbulence," *Journal of Fluid Mechanics* **941**, A34 (2022).
- ¹⁷C. Federrath, J. Roman-Duval, R. S. Klessen, W. Schmidt, and M.-M. Mac Low, "Comparing the statistics of interstellar turbulence in simulations and observations-Solenoidal versus compressive turbulence forcing," *Astronomy & Astrophysics* **512**, A81 (2010).
- ¹⁸J. P. John, D. A. Donzis, and K. R. Sreenivasan, "Solenoidal scaling laws for compressible mixing," *Physical Review Letters* **123**, 224501 (2019).
- ¹⁹V. Eswaran and S. B. Pope, "An examination of forcing in direct numerical simulations of turbulence," *Computers & Fluids* **16**, 257–278 (1988).
- ²⁰M. N. Lemaster and J. M. Stone, "Dissipation and heating in supersonic hydrodynamic and MHD turbulence," *The Astrophysical Journal* **691**, 1092 (2009).
- ²¹C. Seror, P. Sagaut, C. Bailly, and D. Juvé, "On the radiated noise computed by large-eddy simulation," *Physics of Fluids* **13**, 476–487 (2001).
- ²²E. D. Siggia and G. Patterson, "Intermittency effects in a numerical simulation of stationary three-dimensional turbulence," *Journal of Fluid Mechanics* **86**, 567–592 (1978).
- ²³D. Carati, S. Ghosal, and P. Moin, "On the representation of backscatter in dynamic localization models," *Physics of Fluids* **7**, 606–616 (1995).
- ²⁴A. Witkowska, D. Juvé, and J. G. Brasseur, "Numerical study of noise from isotropic turbulence," *Journal of Computational Acoustics* **5**, 317–336 (1997).
- ²⁵T. S. Lundgren, "Linearly forced isotropic turbulence," *Annual Research Briefs (Center for Turbulence Research, Stanford)*, 461–473 (2003).
- ²⁶C. Rosales and C. Meneveau, "Linear forcing in numerical simulations of isotropic turbulence: Physical space implementations and convergence properties," *Physics of Fluids* **17**, 095106 (2005).
- ²⁷M. R. Petersen and D. Livescu, "Forcing for statistically stationary compressible isotropic turbulence," *Physics of Fluids* **22**, 116101 (2010).
- ²⁸S. Stanley, S. Sarkar, and J. Mellado, "A study of the flow-field evolution and mixing in a planar turbulent jet using direct numerical simulation," *Journal of Fluid Mechanics* **450**, 377–407 (2002).
- ²⁹E. R. Hawkes, O. Chatakonda, H. Kolla, A. R. Kerstein, and J. H. Chen, "A petascale direct numerical simulation study of the modelling of flame wrinkling for large-eddy simulations in intense turbulence," *Combustion and Flame* **159**, 2690–2703 (2012).
- ³⁰J. F. Hawley, C. F. Gammie, and S. A. Balbus, "Local three-dimensional magnetohydrodynamic simulations of accretion disks," *The Astrophysical Journal* **440**, 742 (1995).
- ³¹V. Prat, J. Guilet, M. Viallet, and E. Müller, "Shear mixing in stellar radiative zones-II. Robustness of numerical simulations," *Astronomy & Astrophysics* **592**, A59 (2016).
- ³²D. Buaria, E. Bodenschatz, and A. Pumir, "Vortex stretching and entropy production in high reynolds number turbulence," *Physical Review Fluids* **5**, 104602 (2020).
- ³³M. Lee and R. D. Moser, "Direct numerical simulation of turbulent channel flow up to," *Journal of Fluid Mechanics* **774**, 395–415 (2015).
- ³⁴K. J. Rah, C. Dhandapani, and G. Blanquart, "Derivation of a realistic forcing term to reproduce the turbulent characteristics of round jets on the centerline," *Physical Review Fluids* **3**, 084606 (2018).
- ³⁵A. Elnahas, A. Lozano-Duran, and P. Moin, "Toward a Flow-structure-based wall-modeled large-eddy simulation paradigm," *Center for Turbulence Research, Annual Research Briefs*, 59–71 (2020).
- ³⁶J. F. MacArt, J. Sirignano, and J. B. Freund, "Embedded training of neural-network subgrid-scale turbulence models," *Physical Review Fluids* **6**, 050502 (2021).
- ³⁷J. Sirignano and J. F. MacArt, "Dynamic Deep Learning LES Closures: Online Optimization With Embedded DNS," *arXiv preprint arXiv:2303.02338* (2023).
- ³⁸C. Towery, S. Walters, S. Guzik, X. Gao, and P. Hamlington, "A scaling law for the required transition zone depth in hybrid LES-DNS," *Journal of Turbulence* **21**, 722–734 (2020).
- ³⁹J. Christopher, S. M. Guzik, and X. Gao, "High-order implicit-explicit additive Runge-Kutta schemes for numerical combustion with adaptive mesh refinement," *International Journal for Numerical Methods in Fluids* **94**, 1082–1110 (2022).
- ⁴⁰K. M. Waldron, J. Paegle, and J. D. Horel, "Sensitivity of a spectrally filtered and nudged limited-area model to outer model options," *Monthly Weather Review* **124**, 529–547 (1996).
- ⁴¹H. von Storch, H. Langenberg, and F. Feser, "A spectral nudging technique for dynamical downscaling purposes," *Monthly Weather Review* **128**, 3664–3673 (2000).
- ⁴²R. Radu, M. Déqué, and S. Somot, "Spectral nudging in a spectral regional climate model," *Tellus A: Dynamic Meteorology and Oceanography* **60**, 898–910 (2008).
- ⁴³P. C. Di Leoni, A. Mazzino, and L. Biferale, "Inferring flow parameters and turbulent configuration with physics-informed data assimilation and spectral nudging," *Physical Review Fluids* **3**, 104604 (2018).
- ⁴⁴P. Clark Di Leoni, A. Mazzino, and L. Biferale, "Synchronization to big data: Nudging the Navier-Stokes equations for data assimilation of turbulent flows," *Physical Review X* **10**, 011023 (2020).
- ⁴⁵Y. Hasegawa, N. Onodera, Y. Asahi, T. Ina, T. Imamura, and Y. Idomura, "Continuous data assimilation of large eddy simulation by lattice Boltzmann method and local ensemble transform Kalman filter (LBM-LETKF)," *Fluid Dynamics Research* **55**, 065501 (2023).
- ⁴⁶W. W. Grabowski and P. K. Smolarkiewicz, "CRCP: A cloud resolving convection parameterization for modeling the tropical convecting atmosphere," *Physica D: Nonlinear Phenomena* **133**, 171–178 (1999).
- ⁴⁷W. W. Grabowski, "An improved framework for superparameterization," *Journal of the Atmospheric Sciences* **61**, 1940–1952 (2004).
- ⁴⁸P. Yeung and K. Ravikumar, "Advancing understanding of turbulence through extreme-scale computation: Intermittency and simulations at large problem sizes," *Physical Review Fluids* **5**, 110517 (2020).
- ⁴⁹A. Y. Poludnenko and E. S. Oran, "The interaction of high-speed turbulence with flames: Global properties and internal flame structure," *Combustion and Flame* **157**, 995–1011 (2010).
- ⁵⁰P. Colella, "Multidimensional upwind methods for hyperbolic conservation laws," *Journal of Computational Physics* **87**, 171–200 (1990).
- ⁵¹J. Saltzman, "An unsplit 3D upwind method for hyperbolic conservation laws," *Journal of Computational Physics* **115**, 153–168 (1994).
- ⁵²P. Colella and P. R. Woodward, "The piecewise parabolic method (PPM) for gas-dynamical simulations," *Journal of Computational Physics* **54**, 174–201 (1984).
- ⁵³D. A. Donzis and P. K. Yeung, "Resolution effects and scaling in numerical simulations of passive scalar mixing in turbulence," *Physica D* **239**, 1278–1287 (2010).
- ⁵⁴S. Jagannathan and D. A. Donzis, "Reynolds and Mach number scaling in solenoidally-forced compressible turbulence using high-resolution direct numerical simulations," *Journal of Fluid Mechanics* **789**, 669–707 (2016).
- ⁵⁵P. Yeung, K. Sreenivasan, and S. Pope, "Effects of finite spatial and temporal resolution in direct numerical simulations of incompressible isotropic turbulence," *Physical Review Fluids* **3**, 064603 (2018).
- ⁵⁶C. Towery, A. Poludnenko, J. Urzay, J. O'Brien, M. Ihme, and P. Hamlington, "Spectral kinetic energy transfer in turbulent premixed reacting flows," *Physical Review E* **93**, 053115 (2016).
- ⁵⁷J. O'Brien, C. A. Towery, P. E. Hamlington, M. Ihme, A. Y. Poludnenko, and J. Urzay, "The cross-scale physical-space transfer of kinetic energy in turbulent premixed flames," *Proceedings of the Combustion Institute* **36**, 1967–1975 (2017).
- ⁵⁸C. Towery, A. Poludnenko, J. Urzay, M. Ihme, and P. Hamlington, "Spectral energy dynamics in premixed flames," in *Center for Turbulence Research Proceedings of the Summer Program* (2014) pp. 159–168.
- ⁵⁹R. W. Daniels, "Approximation methods for electronic filter design: with applications to passive, active, and digital networks," (No Title) (1974).
- ⁶⁰S. Bose, P. Moin, and F. Ham, "Explicitly filtered large eddy simulation on unstructured grids," *Center of Turbulence Research Annual Research Briefs*, 87–96 (2011).
- ⁶¹M. Germano, "Differential filters for the large eddy numerical simulation of turbulent flows," *Physics of Fluids* **29**, 1755–1757 (1986).
- ⁶²A. Edoh, N. L. Mundis, A. R. Karagozian, and V. Sankaran, "Discrete Filtering Formulations for Large-Eddy Simulations," in *46th AIAA Fluid Dynamics Conference* (2016) p. 3794.
- ⁶³P. Marbaix, H. Gallée, O. Brasseur, and J.-P. van Ypersele, "Lateral boundary conditions in regional climate models: a detailed study of the

- relaxation procedure,” *Monthly Weather Review* **131**, 461–479 (2003).
- ⁶⁴J. C. P. Campuzano, “Trigonometric Interpolation using the Discrete Fourier Transform,” *North American GeoGebra Journal* **10**, 1–13 (2022).
- ⁶⁵A. Zygmund, *Trigonometric series*, Vol. 1 (Cambridge university press, 2002).
- ⁶⁶L.-P. Wang, S. Chen, J. G. Brasseur, and J. C. Wyngaard, “Examination of hypotheses in the Kolmogorov refined turbulence theory through high-resolution simulations. Part 1. Velocity field,” *Journal of Fluid Mechanics* **309**, 113–156 (1996).
- ⁶⁷Y. Zhou, “Interacting scales and energy transfer in isotropic turbulence,” *Physics of Fluids A: Fluid Dynamics* **5**, 2511–2524 (1993).
- ⁶⁸M. Adams, P. Colella, D. T. Graves, J. Johnson, N. Keen, T. J. Ligoeki, D. F. Martin, P. McCorquodale, D. Modiano, P. Schwartz, T. Sternberg, and B. V. Straalen, “Chombo software package for AMR applications design document,” Available at the Chombo website: <http://seesar.lbl.gov/ANAG/chombo/>(September 2008) **2** (2021).
- ⁶⁹W. Zhang, A. Almgren, M. Day, T. Nguyen, J. Shalf, and D. Unat, “Boxlib with tiling: An adaptive mesh refinement software framework,” *SIAM Journal on Scientific Computing* **38**, S156–S172 (2016).
- ⁷⁰M. T. Henry de Frahan, J. S. Rood, M. S. Day, H. Sitaraman, S. Yellapantula, B. A. Perry, R. W. Grout, A. Almgren, W. Zhang, J. B. Bell, *et al.*, “Pelec: An adaptive mesh refinement solver for compressible reacting flows,” *The International Journal of High Performance Computing Applications* **37**, 115–131 (2023).
- ⁷¹M. Vanella, A. Posa, and E. Balaras, “Adaptive mesh refinement for immersed boundary methods,” *Journal of Fluids Engineering* **136**, 040909 (2014).
- ⁷²A. Hay and M. Visonneau, “Adaptive finite-volume solution of complex turbulent flows,” *Computers & Fluids* **36**, 1347–1363 (2007).
- ⁷³N. Ganesh, N. V. Shende, and N. Balakrishnan, “R-parameter: A local truncation error based adaptive framework for finite volume compressible flow solvers,” *Computers & Fluids* **38**, 1799–1822 (2009).
- ⁷⁴T. Plewa, T. J. Linde, V. G. Weirs, *et al.*, *Adaptive mesh refinement, theory and applications* (Springer, 2005).
- ⁷⁵J. M. Stone, T. A. Gardiner, P. Teuben, J. F. Hawley, and J. B. Simon, “Athena: a new code for astrophysical MHD,” *The Astrophysical Journal Supplement Series* **178**, 137 (2008).
- ⁷⁶T. A. Gardiner and J. M. Stone, “An unsplit Godunov method for ideal MHD via constrained transport in three dimensions,” *Journal of Computational Physics* **227**, 4123–4141 (2008).
- ⁷⁷P. E. Hamlington, A. Y. Poludnenko, and E. S. Oran, “Interactions between turbulence and flames in premixed reacting flows,” *Physics of Fluids* **23** (2011).
- ⁷⁸P. E. Hamlington, A. Y. Poludnenko, and E. S. Oran, “Intermittency in premixed turbulent reacting flows,” *Physics of Fluids* **24**, 075111 (2012).
- ⁷⁹Z. Jozefik, M. E. Harvazinski, V. Sankaran, S. S. Dammati, A. Y. Poludnenko, T. Lu, A. R. Kerstein, R. Xu, and H. Wang, “Modeling of high-speed, methane–air, turbulent combustion, Part I: One-dimensional turbulence modeling with comparison to DNS,” *Combustion and Flame* **263**, 113379 (2024).
- ⁸⁰R. Xu, S. S. Dammati, X. Shi, E. S. Genter, Z. Jozefik, M. E. Harvazinski, T. Lu, A. Y. Poludnenko, V. Sankaran, A. R. Kerstein, *et al.*, “Modeling of high-speed, methane–air, turbulent combustion, Part II: Reduced methane oxidation chemistry,” *Combustion and Flame* **263**, 113380 (2024).
- ⁸¹A. Y. Poludnenko, “Pulsating instability and self-acceleration of fast turbulent flames,” *Physics of Fluids* **27**, 014106 (2015).
- ⁸²Y. Kozak, S. S. Dammati, L. G. Bravo, P. E. Hamlington, and A. Y. Poludnenko, “WENO interpolation for Lagrangian particles in highly compressible flow regimes,” *Journal of Computational Physics* **402**, 109054 (2020).
- ⁸³S. S. Dammati, Y. Kozak, C. Rising, J. Reyes, K. A. Ahmed, and A. Y. Poludnenko, “Numerical investigation of the accuracy of particle image velocimetry technique in gas-phase detonations,” *Proceedings of the Combustion Institute* **38**, 3671–3681 (2021).
- ⁸⁴Y. Kozak, S. S. Dammati, L. G. Bravo, P. E. Hamlington, and A. Poludnenko, “Novel Lagrangian-particle tracking method for highly compressible, turbulent, reacting flows,” in *AIAA Scitech 2019 Forum* (2019) p. 1642.
- ⁸⁵J. M. Stone, K. Tomida, C. J. White, and K. G. Felker, “The Athena++ Adaptive Mesh Refinement Framework: Design and Magnetohydrodynamic Solvers,” *The Astrophysical Journal Supplement Series* **249**, 4 (2020).
- ⁸⁶J. M. Stone and T. Gardiner, “A simple unsplit godunov method for multi-dimensional MHD,” *New Astronomy* **14**, 139–148 (2009).
- ⁸⁷D. Donzis, P. Yeung, and K. Sreenivasan, “Dissipation and enstrophy in isotropic turbulence: resolution effects and scaling in direct numerical simulations,” *Physics of Fluids* **20**, 045108 (2008).
- ⁸⁸A. Tsinober, *An informal conceptual introduction to turbulence*, Vol. 483 (Springer, 2009).
- ⁸⁹S. Chen, K. R. Sreenivasan, and M. Nelkin, “Inertial range scalings of dissipation and enstrophy in isotropic turbulence,” *Physical Review Letters* **79**, 1253 (1997).
- ⁹⁰B. W. Zeff, D. D. Lanterman, R. McAllister, R. Roy, E. J. Kostelich, and D. P. Lathrop, “Measuring intense rotation and dissipation in turbulent flows,” *Nature* **421**, 146–149 (2003).
- ⁹¹P. Moin, K. Squires, W. Cabot, and S. Lee, “A dynamic subgrid-scale model for compressible turbulence and scalar transport,” *Physics of Fluids A: Fluid Dynamics* **3**, 2746–2757 (1991).
- ⁹²A. Vreman, “An eddy-viscosity subgrid-scale model for turbulent shear flow: Algebraic theory and applications,” *Physics of Fluids* **16**, 3670–3681 (2004).
- ⁹³Y. Li, C. Meneveau, S. Chen, and G. L. Eyink, “Subgrid-scale modeling of helicity and energy dissipation in helical turbulence,” *Physical Review E* **74**, 026310 (2006).
- ⁹⁴C. Fureby, G. Tabor, H. Weller, and A. Gosman, “A comparative study of subgrid scale models in homogeneous isotropic turbulence,” *Physics of Fluids* **9**, 1416–1429 (1997).
- ⁹⁵U. Piomelli, W. H. Cabot, P. Moin, and S. Lee, “Subgrid-scale backscatter in turbulent and transitional flows,” *Physics of Fluids A: Fluid Dynamics* **3**, 1766–1771 (1991).
- ⁹⁶C. Leith, “Stochastic backscatter in a subgrid-scale model: Plane shear mixing layer,” *Physics of Fluids A: Fluid Dynamics* **2**, 297–299 (1990).
- ⁹⁷T. Aoyama, T. Ishihara, Y. Kaneda, M. Y. K. Itakura, and A. Uno, “Statistics of Energy Transfer in High-Resolution Direct Numerical Simulation of Turbulence in a Periodic box,” *Journal of the Physical Society of Japan* **74**, 3202–3212 (2005).
- ⁹⁸J. A. Domaradzki and R. S. Rogallo, “Local energy transfer and nonlocal interactions in homogeneous, isotropic turbulence,” *Physics of Fluids A: Fluid Dynamics* **2**, 413–426 (1990).
- ⁹⁹J. A. Domaradzki and D. Carati, “An analysis of the energy transfer and the locality of nonlinear interactions in turbulence,” *Physics of fluids* **19** (2007).
- ¹⁰⁰P. Yeung and J. G. Brasseur, “The response of isotropic turbulence to isotropic and anisotropic forcing at the large scales,” *Physics of Fluids A: Fluid Dynamics* **3**, 884–897 (1991).
- ¹⁰¹M. P. Martin, U. Piomelli, and G. V. Candler, “Subgrid-scale models for compressible large-eddy simulations,” *Theoretical and Computational Fluid Dynamics* **13**, 361–376 (2000).
- ¹⁰²D. Veynante and L. Vervisch, “Turbulent combustion modeling,” *Progress in Energy and Combustion Science* **28**, 193–266 (2002).
- ¹⁰³B. Vreman, B. Geurts, and H. Kuerten, “Subgrid-modelling in LES of compressible flow,” *Applied Scientific Research* **54**, 191–203 (1995).
- ¹⁰⁴C. Xie, J. Wang, H. Li, M. Wan, and S. Chen, “A modified optimal LES model for highly compressible isotropic turbulence,” *Physics of Fluids* **30**, 065108 (2018).